Materials Today Chemistry 34 (2023) 101767

Contents lists available at ScienceDirect

Materials Today Chemistry

journal homepage: www.journals.elsevier.com/materials-today-chemistry/

Controllable ion transport in bilayer graphene with charged nanopores

Yanbo Xin [a], Qin Gao [b], Jiangshun Huang [a], Juan Gao [a], Xueli Geng [a], Hongliang Shi [a], Mei Wang [a], Zhisong Xiao [a], Paul K. Chu [c], Anping Huang [a,*]

[a] School of Physics, Beihang University, Beijing, 100191, China
[b] School of Physics and School of Chemistry, Beihang University, Beijing, 100191, China
[c] Department of Physics, Department of Materials Science and Engineering, and Department of Biomedical Engineering, City University of Hong Kong, Tat Chee Avenue, Kowloon, Hong Kong, China

ARTICLE INFO

Keywords:
Ion transport
Bilayer graphene
Asymmetric nanochannels
Nanopores
Ion current rectification

ABSTRACT

Heterogeneous membrane structures exhibiting ion diode effects have attracted significant interest in energy conversion and storage. Herein, asymmetric double-layer graphene stacks with charged nanopores are constructed and placed in a KCl solution to study the controllable ion transport properties. Ion current rectification (ICR) is observed and the switching ratio is up to 10^2 by leveraging the asymmetric structure, charge, and interlayer distance. The trapping behavior of cations (K^+) and anions (Cl^-) in the nanochannels is investigated by applying bias voltages, and peak ion capture occurs at an electric field of $E = 0.02$ V/Å. The underlying mechanism of ICR is elucidated according to the dependence between the ion current and carrier concentration in the nanopores. The results provide valuable insights into the ICR mechanism and reveal high potential in the energy field.

1. Introduction

Inspired by the high permeability and selectivity of biological nanopores, heterogeneous membrane structures based on the ion diode effect have garnered significant interest as promising candidates for osmotic energy conversion and storage [1–4]. The ion transport pathway in the membranes is intentionally constructed with an asymmetric architecture to facilitate both ionic conductivity and charge (cation/anion) selectivity [4–7]. Micrometer-thick asymmetric membranes composed of diverse materials such as polymers [8,9], silica [10,11], alumina [12], have demonstrated the capability for selective ion transport. Although these devices achieve both ionic conductivity and charge selectivity, conventional membrane materials such as polymers and mesoporous carbon suffer from inefficient ion transport due to excessively long ion transport channels [5].

To overcome this limitation, asymmetric nanochannel membranes constructed from metal-organic frameworks (MOFs) [1,13–16], covalent organic frameworks (COFs) [17–22], and two-dimensional materials [23–26] have demonstrated advantages in enhancing the ion flux and output power density by virtue of the ultrashort ion transport paths on the nanoscale. Specifically, two-dimensional materials including graphene possess higher structural and chemical stability than the organic framework, making them competitive in constructing nanochannels. The asymmetric bilayer atomic-scale nanochannels show significant potential in achieving ion current rectification (ICR) at the atomic thickness [24,25]. Single-layer graphene nanopores can acquire charge through atomic polarization, for example, oxygen and boron-substituted graphene [27,28], facilitating their utilization in ion separation. By stacking graphene nanopores with opposing charges, asymmetric nanochannels can be constructed, implying significant prospects for applications in charge selectivity and ion rectification.

In this work, a heterogeneous membrane consisting of bilayer charged graphene is designed for efficient ICR. The influence of the structure, charge asymmetry, and interlayer distance on the ion trapping and transport processes is studied. The ultra-short nanochannel shows a remarkable ion current switching ratio of 10^2, providing evidence of the effective modulation and control of ion transport. The results provide valuable insights into the restricted transport behavior of ions in nanoscale spaces and as well as the design and fabrication of ion diodes.

---

* Corresponding author.
E-mail address: aphuang@buaa.edu.cn (A. Huang).

https://doi.org/10.1016/j.mtchem.2023.101767
Received 24 July 2023; Received in revised form 7 September 2023; Accepted 7 October 2023

2. Computational methods

2.1. First principles calculation

The computation of the electron energy barrier is conducted using the Vienna Ab initio Simulation Package [29] employing the projector augmented wave (PAW) potentials of Perdew-Burke-Ernzerhof (PBE) [30]. The transition state search is performed utilizing the climbing-image nudged elastic band (CI-NEB) method by VASP-VTST [31–34]. A rectangular graphene membrane (12.82×12.34 Å^2) is positioned in a three-dimensional periodic simulation box oriented parallel to the *x-y* plane. The optimized C–C bond length is determined to be 1.424 Å, which closely matched experimental data [35]. In all cases, the Brillouin zone is sampled with a $3 \times 3 \times 1$ *k*-point mesh, except during structural optimization and transition state search where it is set to $1 \times 1 \times 1$. A plane wave cutoff energy of 550 eV was employed for all calculations. Electron energies are converged within a tolerance of 1×10^{-7} eV, and geometric optimization allows all atoms to relax until the force on each atom reached 1×10^{-2} eV/Å. Visualization, structure modeling, and analysis are conducted using the electronic and structural analysis (VESTA) software [36].

2.2. Molecular dynamics simulation

To model ionic currents through a nanopores in bilayer graphene, we constructed a 4×4 array of nanochannels and immersed it in the 0.5 mol/L KCl solution, as shown in Fig. 1 (a). Each nanochannel in the array is composed of a pair of nanopores stacked up and down, as shown in Fig. 1 (b)–(e). The partial atomic charges are determined by the Atom Charge Calculator II (ACC II) utilizing the EQeq method, as illustrated in Fig. S1 [37]. For non-bonded interactions, the mixing rule is employed to determine the Lennard-Jones (LJ) parameters, with the exception of carbon-water interactions, which are characterized by the force-field parameters provided in reference [38]. The LJ parameters can be found in Table S1 of the Supplementary Information. The water molecules are modeled using the TIP3P model [39,40]. The simulation box is a rectangular parallelepiped with dimensions of 8.1 nm $\times$ 8.1 nm $\times$ 10.6 nm and periodic boundary conditions are applied in all directions. In each simulation, an initial energy minimization process is performed with the LAMMPS package [41,42]. Subsequently, the system undergoes equilibration in the NVT ensemble with a constant number of particles, volume, and temperature maintained for a duration of 40 ns at a pressure of 1 atm and temperature of 300 K. It should be noted that the first 4 ns of this period are allocated to the pre-equilibration processes. The vector electric field $\overrightarrow{E}$ intensity is applied to the system, with its direction aligned along the *z*-axis. In the subsequent sections, $E > 0$ V/Å indicates the positive direction along the *z*-axis, while $E < 0$ V/Å represents the negative direction along the *z*-axis.

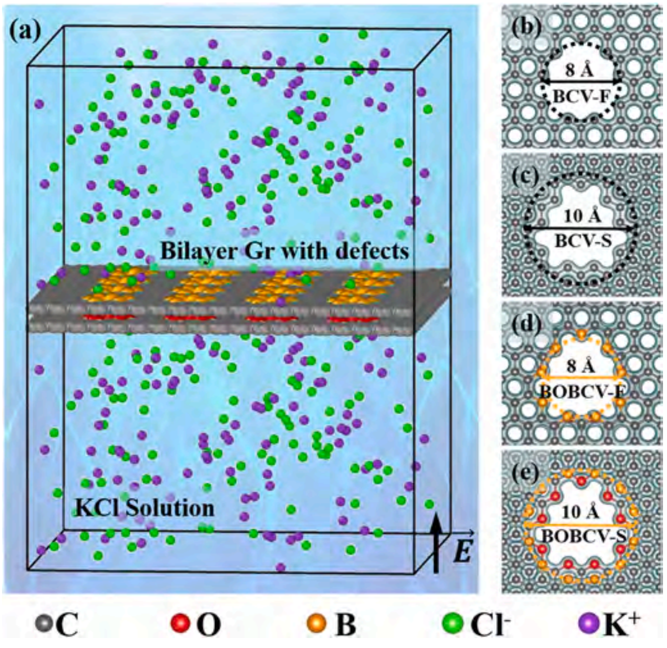

Fig. 1. (a) Simulation system: atoms and ions are represented as van der Waals spheres and water molecules are displayed transparently. Ionic current model of bilayer graphene with nanopores. Perspective view of bilayer graphene with different types of defects: (b) BCV-F, (c) BCV-S, (d) BOBCV-F, and (e) BOBCV-S.

3. Results and discussion

3.1. Nanopores in bilayer graphene

3.1.1. Pristine bilayer graphene

The characteristic of pristine monolayer graphene to block the passage of ions has been studied [43,44] and the ion-blocking behavior is verified in pristine bilayer graphene structures in this section. In the case of bilayer graphene with an AA stacking arrangement, the pristine graphene layers are immersed in the 0.5 mol/L KCl solution, and a positive bias voltage is applied along the direction perpendicular to the graphene plane, as depicted in Fig. 1(a). When a bias is applied in the z direction, K^+ and Cl^- may undergo directed migration under the influence of an electric field, resulting in an ionic current *I*. The equation for the ionic current is shown in the following:

$$I = \sum_i q_i v_i / H, \tag{1}$$

where H is the height of the simulated system and q_i and v_i are the charge and velocity of the $i - th$ ion, respectively. The total charge passing through the nanopores are defined as follows.

$$Q = \int I_t dt \ . \tag{2}$$

The ionic current *I* and the ionic charge *Q* provide direct insights into the ion penetration dynamics within the nanopore.

The cumulative charge of K^+ and Cl^- translocating across the pristine bilayer graphene is consistently maintained at zero, as shown by the green line in Fig. 2 (a). The result shows that K^+ and Cl^- cannot penetrate the pristine bilayer graphene when a bias voltage of 0.03 V/Å is applied within the simulation duration of 40 ns. This behavior strongly proves that the pristine bilayer graphene inhibits the penetration of both K^+ and Cl^-. The closely packed carbon atoms in the bilayer graphene significantly limit the space required for ion transport, thus preventing them from penetrating the materials. These defects facilitate ion mobility and establish the requisite space required for ions to penetrate the bilayer graphene structure. Consequently, these observations emphasize the importance of introducing defects into the structure of bilayer graphene.

3.1.2. Bilayer graphene with nanopores

The emergence of atomic-level carbon vacancies is an inherent and inescapable phenomenon during the fabrication process of graphene, and these defects are potential channels for ion penetration. To investigate the ion transport behavior of atomic-scale defects, bilayer graphene with carbon vacancies for the first (BCV–F) is constructed. In this structure, the upper and lower layers of nanopores are equal in size, about 0.8 nm in diameter, as shown in Fig. 1 (b). BCV-F is immersed in the 0.5 mol/L KCl solution, and a voltage of 0.03 V/Å is applied along the direction perpendicular to the graphene plane, as illustrated in Fig. 1 (a). The charge equilibration analysis confirms that the bilayer graphene with carbon vacancies is electrically neutral, with no charge accumulation at the nanopores, as shown in Fig. S1 (a). The charges of ions

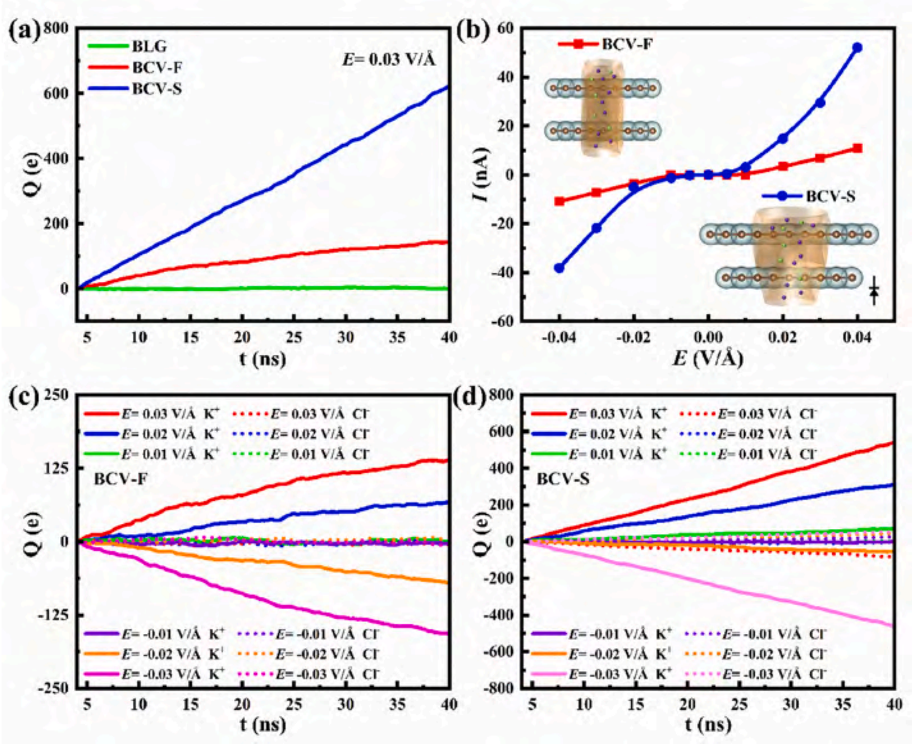

Fig. 2. (a) Ionic currents through BLG, BCV-F, and BCV-S in the 0.5 mol/L KCl solution. (b) Current-voltage (*I*–*V*) characteristics of the bilayer graphene structure that contains defects. The insets represent the schematic diagram of nanochannel and mark the direction of ICR. (c) and (d) provide the detailed representations of the ionic currents for both K^+ and Cl^- in BCV-F and BCV-S, respectively.

passing through the nanopores increase linearly producing a stable ion current. The ion current is the result of the combined action of K^+ and Cl^-, where cations and anions move in opposite directions, respectively, as shown in Fig. 2 (b). The results show that the defective bilayer graphene allows a considerable number of ions to pass through the graphene nanopores, while the pristine bilayer graphene does not. Equal reverse biases are applied to the system, and K^+ currents of equal magnitude but opposite directions are observed. In addition, the conductivity of K^+ is positively correlated with the applied biased voltage, while no significant Cl^- current is detected, as shown in Fig. 2 (c). This phenomenon is attributed to the fact that the hydration radii of K^+ is smaller than that of Cl^-, as shown in Fig. S2 (a), (b), and the hydration radii of ion plays a key role in ion transport in the confined space of ~1 nm.

BCV-F with the symmetrical structure does not exhibit the ionic rectification behavior, as shown by the red line in Fig. 2 (b). At a bias voltage of ±0.01 V/Å, there is no ion penetration through the nanopores, and ion trapping near the nanopores is negligible. By increasing the positive bias, ion trapping in the nanopores initially increases and then decreases, as shown in Fig. S3 (a). Furthermore, it is found that K^+ and Cl^- are trapped in the lower-layer and upper-layer nanopores, respectively, leading to an ion current blocking phenomenon. The phenomenon is disrupted as the external bias voltage exceeds 0.04 V/Å, leading to a decrease in ion trapping, as shown in Fig. S3 (a). Based on the results, the introduction of nanopores in bilayer graphene membranes provides the possibility for the penetration of K^+ and Cl^- and ion currents. BCV-F is a symmetrical nanochannel and so ions are transported through these symmetrical channels under an external bias without ICR.

3.2. *Ion transport of different nanopores*

3.2.1. *Asymmetric nanopores*

By changing the shape and size of the transport channel, the ion transport channel can effectively control ion transport [45,46]. To generate the ICR in the nanochannel, structural asymmetry is introduced into the bilayer graphene with carbon vacancies so that the nanopore sizes in the upper and lower graphene layers are different. Bilayer graphene with carbon vacancies for the second (BCV–S), where the upper graphene nanopores exhibit a larger size (1 nm in diameter) than the lower one (0.8 nm in diameter), as shown in Fig. 1 (c), is verified to be electrically neutral by the charge equilibration analysis, as illustrated in Fig. S1 (b). BCV-S is submerged in the 0.5 mol/L KCl solution, and different voltages are applied perpendicular to the plane of the graphene, as shown in Fig. 1 (a). The findings show that the incorporation of an asymmetrical structure exerts a significant regulatory impact on ion transport and trapping in both symmetric BCV-F and asymmetric BCV-S.

Three distinct phenomena have been observed from the symmetric BCV-F and asymmetric BCV-S: (1) ICR, (2) dominant carriers, and (3) voltage-dependent ion trapping. Firstly, the asymmetric BCV-S system shows the ICR, but the symmetric BCV-F system does not. Especially in the range of $-0.02\ V/Å \leq E \leq 0.02\ V/Å$, the forward ion current significantly exceeds the reverse ion current, as indicated by the blue line in Fig. 2 (b). The generation of ICR in BCV-S is related to the uneven distribution of K^+ ions under the opposite bias near the nanopores, in which K^+ ions are still the mainstream carrier in this process. Under positive bias, K^+ ions pass through small defects and then through large defects in turn, while under negative bias, the order is opposite. The obstacle for K^+ ions to penetrate the nanopore comes from the obstruction of two nanopores with different sizes and the small nanopore has a greater influence on the potassium ion flow. Under positive bias, the lower side of smaller nanopore is enriched by K^+ ions, and K^+ ions are easily drawn by external bias to form K^+ ion flow. On the contrary, under negative bias, the K^+ ion on the upper side of the smaller nanopore is in a barren state, and the K^+ ion current is weak due to the lack of K^+ ion source. Therefore, the uneven distribution of upstream K^+ ions concentration caused by positive bias and negative bias when penetrating smaller nanopore is the main reason for ICR effect in BCV-S. Under the condition of $|E| > 0.02$ V/Å, the ICR effect is not obvious. In this condition, the forward current is approximately equal to the negative current, as shown by the blue line in Fig. 2 (b). And the K^+ ions get enough energy, and the concentration difference near the pinhole is no longer the main influencing factor. Secondly, the ion types of carriers are affected by the size of nanopores. BCV-S provides larger transport space for Cl^-, allowing them to participate in ion conduction, as shown in Fig. 2 (d). It is worth noting that in BCV-S system, the same as BCV-F, K^+ ions are the main carriers, which is determined by the ion radii of the two ions. Thirdly, in the symmetric BCV-F, trapping of K^+ and Cl^- increases initially, reaches a peak, and then decreases as the voltage is increased. This is attributed to the accumulation of ions in the symmetric pore structure, impeding transport of ions with opposite charges. However, when the bias exceeds 0.04 V/Å, the accumulation effect is overcome, and the external voltage becomes the dominant factor in ion transport, leading to a gradual reduction in ion accumulation, as shown in Fig. S3 (a). In the asymmetric BCV-S system, this blocking phenomenon is overcome and no peak is observed, as shown in Fig. S3 (b). Therefore, introducing structural asymmetry is crucial to modulating ion current rectification in the design of ultra-thin nanofluidic systems.

3.2.2. Charged nanopores

Introduction of atoms or functional groups to the edges of graphene nanopores enables the nanopores to acquire charges, thereby achieving functionalization for nanopore particle sieving [47]. The current investigation adopts a model distinguished by a charge asymmetric bilayer structure. This bilayer graphene consists of a stacked configuration featuring O-terminal and B-terminal carbon vacancies for the first (BOBCV–F), and the diameter of the nanopore is about 0.8 nm, as shown in Fig. 1 (d). Upon immersion in an aqueous solution, the bilayer graphene defect structure adopts a symmetric nanochannel configuration, wherein the upper layer is composed of positively charged nanopore defects (B) and the lower layer consists of negatively charged nanopore defects (O), as illustrated in Fig. 1 (a). In BOBCV-F, the lower-layer oxygen atom obtains electrons from adjacent carbon atoms to produce a negative charge (~−0.23 e). Similarly, the upper-layer boron atoms lose electrons to neighboring carbon atoms resulting in a positive charge (~+0.89 e), as shown in Fig. S1 (e).

The transition from the uncharged BCV-F configuration to the charged BOBCV-F configuration leads to the following alterations in ion transport. Firstly, ICR is observed from BOBCV-F when a positive bias is applied along the z-axis, while a negative bias is applied in the opposite direction. By varying the applied bias to $E = 0.01$, 0.02, 0.03, and 0.04 V/Å, the ion current is observed to traverse through the nanopore defects, as shown in Fig. 3 (a). Conversely, when reversing the bias with values of $E = -0.01$, -0.02, -0.03, and -0.04 V/Å, no significant ion current is observed through the nanopores in the BOBCV-F system, as shown in Fig. 3 (a). Under different ion biases, the ion switching ratio of the BOBCV-F system increases with the absolute value of the biased voltage, as demonstrated in Fig. S5. Secondly, significant changes in the dominant ion carriers are observed at a positive bias. In the case of BCV-F, K^+ ions are found to serve as the primary carrier, as shown in Fig. 2 (c). Conversely, in the charged nanopore defects BOBCV-F, a shift occurs and Cl^- ions emerge as the predominant carrier, as shown in Fig. S6 (a). For nanopore defects of the same size, the positively charged boron atoms in the upper layer exert a stronger repulsive effect on K^+ than the negatively charged oxygen atoms in the lower layer. Therefore, only Cl^- ions participate in the conduction in this system. Thirdly, as the positive bias increases, the generated forward ion current does not increase linearly with the bias magnitude. Particularly, at $E = 0.02$, 0.03, and 0.04 V/Å, there is no significant change in the ion currents, as shown in Fig. 3 (a). This can be attributed to that the K^+ ions are initially trapped and accumulated by the lower-layer nanopore defects (O) at a positive

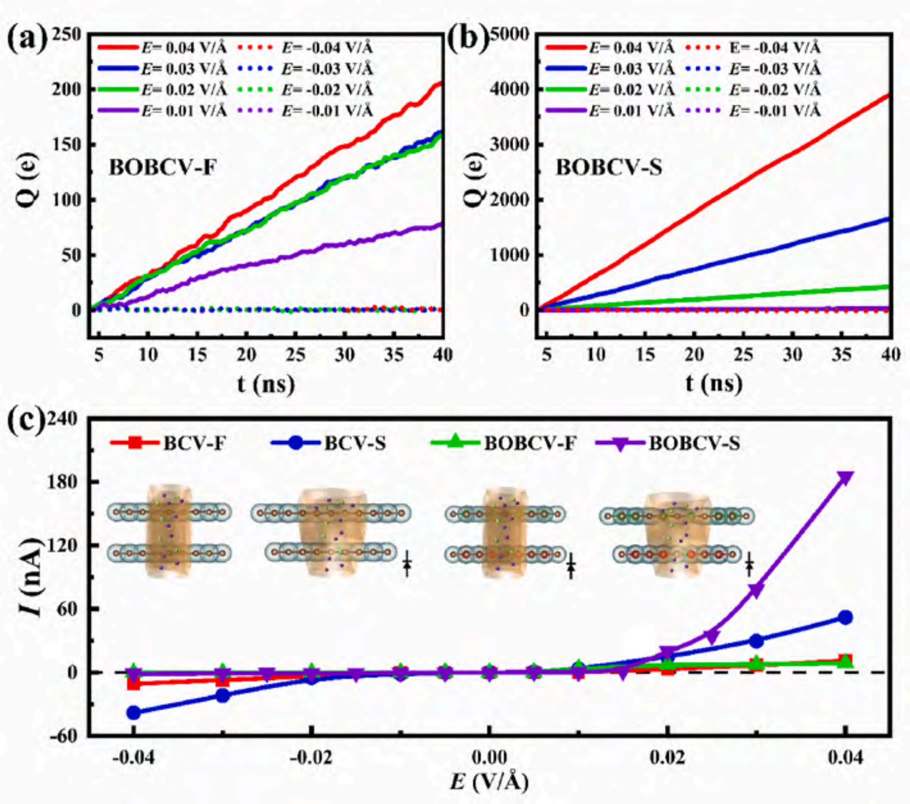

Fig. 3. Ionic currents through (a) BOBCV-F and (b) BOBCV-S in the 0.5 mol/L KCl solution. (c) Current-voltage (*I–V*) characteristics of the bilayer graphene structure that contains defects. The insets represent the schematic diagram of nanochannel and mark the direction of ICR for bilayer graphene with different types of defects: BCV-F, BCV-S, BOBCV-F, and BOBCV-S, respectively.

bias. They are unable to overcome the barrier created by the positively charged upper-layer nanopore defects (B). With increasing voltages, accumulation of K^+ ions in the lower-layer nanopore increases, as shown in Fig. 4 (a), but the behavior of Cl^- differs. At a positive bias, they accumulate in the upper-layer nanopore defect (B) and can penetrate the lower-layer negatively charged nanopore defects (O) under the influence of the electric field. As the bias increases, penetration of Cl^- through the lower-layer nanopore becomes faster. The amount of Cl^- trapped in the upper nanopores gradually decreases, mainly due to the inability of the upper nanopores to trap Cl^- in a timely manner. This is the main reason why the ion current does not increase proportionally with increasing bias.

To facilitate comprehension of the ion transport behavior, calculations are conducted to determine the ion density in the BOBCV-F system at different voltages. The relative ion density, denoted as ρ, is computed along the z-axis at an interval of "0.1 Å" across each plate, with the center positions of the two graphene nanosheets within the pore defining the origin of the z-coordinate, as depicted in Fig. 4 (a). For bias voltages $E \leq 0$ V/Å, no ion trapping is observed in the nanopores of the upper and lower graphene layers at the z-axis coordinates of approximately −1.9 and 1.9, respectively, as shown in Fig. 4 (a). With increasing negative biases, K^+ and Cl^- ions are enriched outside the upper graphene layer and the lower graphene layer, respectively. When $E > 0$ V/Å, Cl^- trapping in the bilayer Graphene nanopore gradually decreases, while K^+ trapping increases. It is worth noting that under a positive bias voltage, only Cl^- ions participate in ion conduction in the BOBCV-F structure, but K^+ ions do not. Consequently, it can be concluded that obstruction of K^+ penetration by the upper B-terminal nanopore results in the accumulation of K^+ being trapped in the lower O-terminal nanopore as the external bias voltage is gradually augmented.

3.2.3. Hybrid nanopores

It is evident that the structure and morphology of bilayer graphene nanopores as well as the existence of charge asymmetry play a regulatory role in ion transport. Considering that the BOBCV-F exhibits a strong blocking effect on K^+ due to the presence of the upper-layer boron termination, only Cl^- ions act as carriers and suppress the contribution of K^+ in ion rectification. To address the issue, a hybrid defect, namely

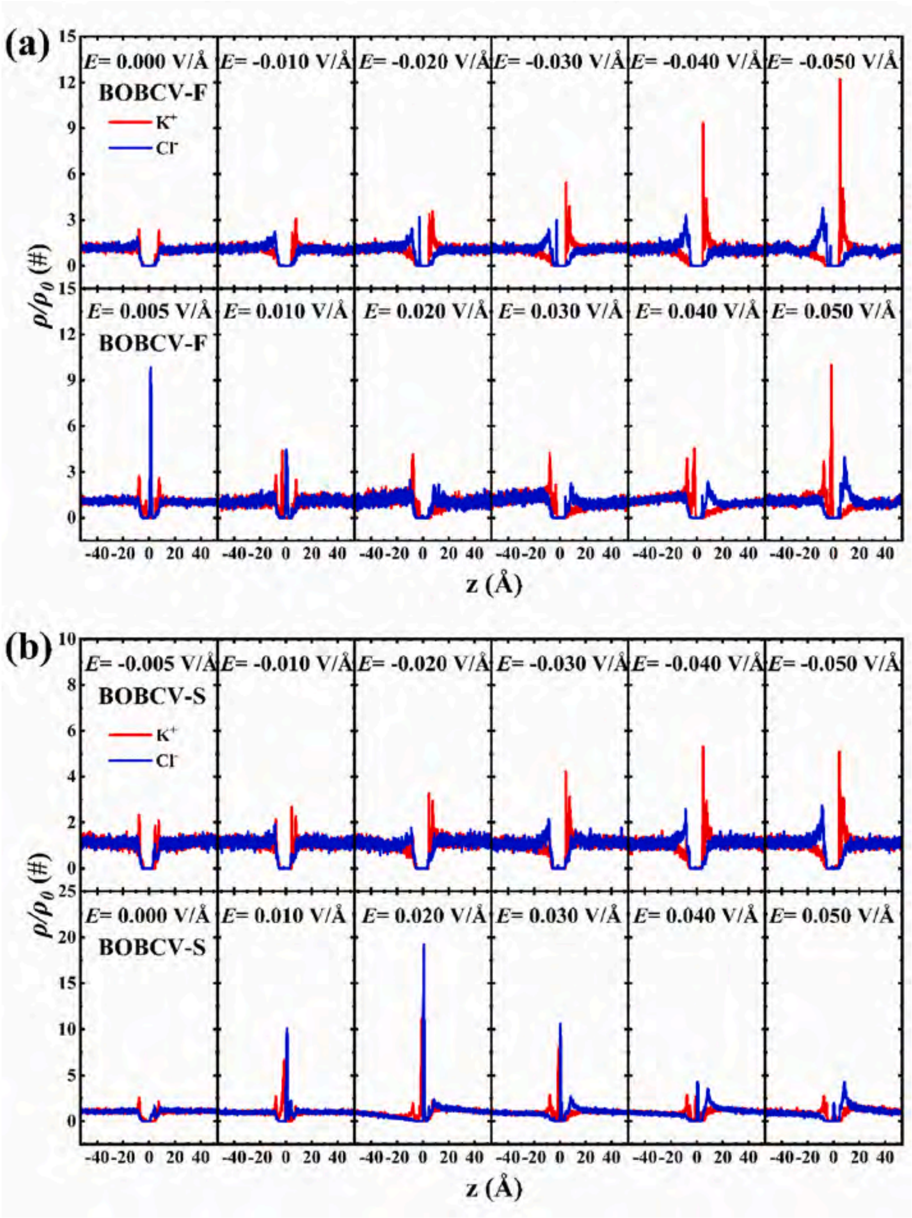

Fig. 4. Distribution of ions along the z-direction through (a) BOBCV-F and (b) BOBCV-S at different applied biases.

bilayer graphene consisting of a stacked configuration featuring O-terminal and B-terminal carbon vacancy in the second (BOBCV–S), is devised to combine the structure and morphology of the nanopore with a charged asymmetry. In this system, the size of the upper B-terminated nanopore is increased to 1.0 nm in diameter and the size of the lower O-terminated nanopore is 0.8 nm in diameter, as shown in Fig. 1 (e). By placing this bilayer graphene defect structure in an aqueous solution, an asymmetric nanochannel is formed to consist of the up-layer positively charged nanopore defects (B) and low-layer negatively charged nanopore defects (O), as shown in Fig. 1 (a). In the charged BOBCV-S, the lower-layer oxygen atoms obtain electrons from adjacent carbon atoms, resulting in a negative charge (~ -0.24 e). Similarly, the upper-layer boron atoms lose electrons to adjacent carbon atoms to produce a positive charge ($\sim +0.81$ e), as shown in Fig. S1 (f). It is noted that the nanopore with the up-layer boron termination has a larger size than the nanopore terminated with oxygen in the low-layer.

By increasing the size of the nanopore terminated with upper-layer boron atoms, the distribution of nanopore charges is altered, resulting in a significant modulation of the transport behavior of the K^+ and Cl^- ion currents. Firstly, BOBCV-S exhibits ICR when subjected to vertical positive and vertical negative biases along the z-axis, as illustrated in Fig. 3 (b), (c). Application of biases with values of $E = 0.01$, 0.02, 0.03, and 0.04 V/Å facilitates the passage of ion currents through the nanopore defect. Conversely, under reverse biases of $E = -0.01$, -0.02, -0.03, and -0.04 V/Å, no substantial ion current flows through the bilayer graphene nanopore defect, as observed in Fig. 3 (b). Across a range of diverse bias voltages, the ion rectification ratio consistently remains at a significantly elevated level, with certain specific bias voltages demonstrating an ion switching ratio exceeding 10^2, as shown in Fig. S5 (d). These findings suggest that the nanopore system has excellent fluidic diode characteristics. Secondly, under positive bias conditions, both K^+ and Cl^- participate in ion conduction leading to an increased conduction of ion currents. It is observed that BOBCV-S allows a significant amount of K^+ to pass through the nanopore under forward biases ($E = 0.01$, 0.02, 0.03, and 0.04 V/Å), as shown in Fig. S6 (b). This phenomenon is not observed from BOBCV-F, as shown in Fig. S6 (a). In particular, under positive biases, especially $E = 0.02$, 0.03, and 0.04 V/Å, BOBCV-S exhibits an approximately five-fold increase in ion conduction compared to BOBCV-F, as shown in Fig. 3 (c). Thirdly, with increasing positive bias, a linear increase in the generated forward ion current is observed. Under the applied bias ($E = 0.005$, 0.01, and 0.015 V/Å), no significant ion current is observed from the BOBCV-S system. A linear increase in the ion current is observed with increasing applied bias ($E = 0.02$, 0.03, and 0.04 V/Å), as shown in Fig. 3(b), (c), while no ion current blockade is observed.

In the BOBCV-S system, both K^+ and Cl^- contribute to the ion current. For bias voltages $E \leq 0$ V/Å, no ion trapping is observed in the nanopores of the upper and lower graphene layers at z-axis coordinates of approximately -1.9 Å and 1.9 Å, respectively, as shown in Fig. 4 (a). With increasing negative biases, K^+ and Cl^- are enriched on the outer side of the upper graphene layer and outer side of the lower graphene layer, respectively, where the process is similar to that observed from the BOBCV-F system. When the electric field is greater than zero ($E > 0$ V/Å), trapping of Cl^- and K^+ increases initially, peaks, and then decreases. Trapping of Cl^- and K^+ initially increase, reaches a peak, and then decreases again at a positive bias voltage. When $0 < E < 0.02$ V/Å, both K^+ and Cl^- contribute to conduction, and ion trapping increases with increasing voltages. When $E > 0.02$ V/Å, K^+ and Cl^- ions conduct, and the ions are carried away from the nanopores by the external electric field. Considering the variations of K^+ and Cl^- with bias voltages in both the BOBCV-F and BOBCV-S systems, ion trapping increases with voltages before ion conduction occurs. Once ion conduction is established, replenishment of ions decreases with the voltage.

The prominent unidirectional ions transport of atomic scale membranes makes them ideal candidates for electrochemical energy conversion. The osmotic energy is generated by separating two cells containing salt solutions of different concentrations using ion-conductive membranes. At the interface of these two solutions, an electrochemical gradient occurs and drives ions across the membrane, generating an osmotic ion flux. In BOBCV-S systems, cations/anions move in opposite directions, resulting in net osmotic current, in which both K^+ and Cl^- contribute to ion current. Among them, the double ion channel has more advantages than the anion exchange membrane and cation exchange membrane, which only allow a single charged ion to penetrate.

3.2.4. *Interlayer distance*

The transport behavior of ions can be influenced by the interlayer distance of bilayer graphene through methods such as intercalation, solvent effects, applied pressure, or etching [48]. By expanding the study of ion transport modulation in BOBCV-S, the influence of augmenting the interlayer distance of bilayer graphene on the ion transport is investigated. The interlayer distance of BOBCV-S, initially set at 3.8 Å, is adjusted to 7.6 Å. This bilayer graphene defect structure is immersed in the 0.5 mol/L KCl solution, and a positive bias and a negative bias are applied along the z-direction.

Adjusting the gap between the layers of the BOBCV-S changes the ion transport and trapping behavior. Firstly, under the same bias conditions, the ion current of the system increases. Upon applying a bias of $E = 0.02$ V/Å, the K^+ ion current increases by approximately three times, while the Cl^- ion current switches from a closed state to an open state, as shown in Fig. 5(a), (b). When a bias of $E = -0.02$ V/Å is applied, both the K^+ and Cl^- ion currents remain at low levels, with few charge carriers penetrating the nanopore defects. Secondly, under a positive bias of $E = 0.02$ V/Å, the augmented interlayer distance facilitates interlayer ion trapping, as illustrated in Fig. 5 (e), (f). In contrast, at a negative bias of $E = -0.02$ V/Å, the increased interlayer distance does not result in interlayer ion trapping, as shown in Fig. 5 (c), (d). The quantity of interlayer ion trapping directly influences the ion current under positive biasing, leading to a further increase in the forward conduction current. This characteristic, wherein the forward ion current increases while the reverse current is suppressed, holds significant importance in enhancing the permeability of semipermeable membranes while maintaining high selectivity. Thirdly, a similar observation can be made under a positive bias of $E = 0.02$ V/Å, wherein an increased interlayer distance leads to an extended duration to reach the peak ion trapping. For BOBCV-S with an interlayer distance of 3.8 Å, the saturation time in the nanopore is approximately 1.5 ns, as shown in Fig. S7 (a). In contrast, for BOBCV-S with an interlayer distance of 7.6 Å, the saturation time in the nanopore is approximately 10 ns, as shown in Fig. S8 (a). Following a continuous thermal equilibration period of 40 ns in the simulation, the applied bias is removed, resulting in the de-trapping of ions within the nanopores and return to the solution, as illustrated in Fig. S7 (b) and S8 (b).

Increasing the interlayer distance in bilayer graphene nanopore defects yields augmented ion currents and interlayer ion trapping under positive bias, while concurrently preserving diminishing the currents under negative bias. This behavior has potential in improving the permeability and selectivity of semipermeable membranes. Additionally, a larger interlayer distance increases the time to reach the peak ion trapping, indicating the importance of interlayer distance in controlling the ion dynamics in the nanopores.

3.3. *Ion transport mechanism*

To elucidate the underlying mechanism of ICR, the distribution of ion concentration in the nanopores of BOBCV-S is investigated under various bias voltages. Initially, in the absence of an external electric field ($E = 0$ V/Å), the nanopores have a limited population of K^+ and Cl^- due to random collisions with water molecules in the solution. At a positive external electric field of $E = 0.02$ V/Å, the ion concentration in the nanopore goes up but at a negative external electric field of $E = -0.02$ V/Å, the ion concentration decreases. The influence of the applied bias

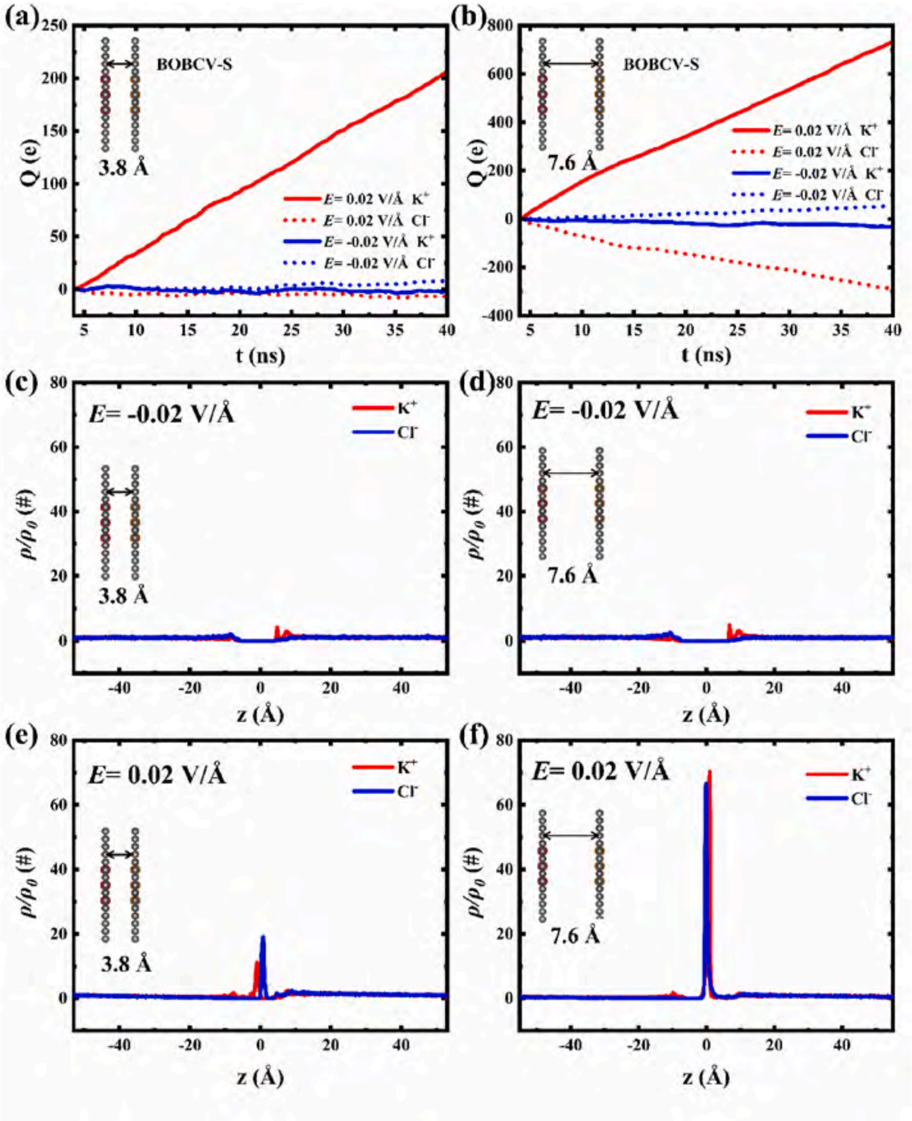

Fig. 5. (a) Ionic currents through BOBCV-S and (b) double interlayer distance BOBCV-S in the 0.5 mol/L KCl solution. (c) and (e) Distributions of ions along the z-direction in the BOBCV-S system at biased voltages of −0.02 and 0.02V/Å. (d) and (f) Distribution of ions along the *z*-direction in the BOBCV-S system with a double distance at biased voltages of −0.02 and 0.02V/Å.

voltage on the charge carrier population is shown in Fig. 6 (a) - (f). This ICR behavior can be applied to a wider range of nanoscale bilayer asymmetric ion transport channels, as shown in Fig. 6 (g)–(i). These observations highlight the impact of the applied bias voltage on the ion concentration distribution in the nanopore and reveal the intrinsic mechanism of ion rectification in the asymmetric nanopore system.

Furthermore, the ion transport process in charged nanopores is investigated using the climbing image-nudged elastic band (CI-NEB) technique, revealing that the carrier distribution in the nanopore is controlled by the functional nanopores. These charged nanopores provide adsorption sites and transport paths for counterions [49,50]. When an ion vertically penetrates a charged nanopore, it generates an energy well or barrier at counter-charged nanopores or co-charged nanopores, respectively, as shown in Fig. 7 (a) and (b). The graphene layer characterized by an energy potential well that can trap counter-ions is called a trapping layer, while the graphene layer characterized by an energy barrier that can repel co-ions is called a barrier layer. Charged graphene nanopores only allow counter-ion penetration, but not co-ion penetration, as shown in Fig. S9 (a)–(f). When stacking the two charged layers together, K^+ and Cl^- exhibit energy barriers within nanopores with the same charge, while they exhibit energy wells within nanopores with opposite charges, as shown in Fig. 7 (c). Such functionalized nanopores with opposite charges induce anions and cations to be adsorbed on both sides of the nanochannel respectively, which provides a carrier concentration difference for ICR generation.

The ionic current is determined by the salt ion concentration of K^+ and Cl^- in the nanopores of the bilayer graphene nanochannels. The ion concentration in the nanopores depends not only on the concentration of electrolytes in the solution pool, but also on the structure and charge asymmetry of the nanopores. The charges inside the nanopores, as described by the classical Debye double-layer theory, play a crucial role in the ion concentration distribution in the pore and consequently, the conductivity of the solution. Graphene with charged nanopores selectively traps counter-ions, and the trapping behavior leads to enough carriers passing through the nanopores to form ion currents. The direction and magnitude of ion current conduction are determined by the placement of two atomic layers with opposite charges. Ions tend to be trapped by the trapping layer first and then penetrate the barrier layer under the external electric field. This behavior determines the direction of current flow in the fluid diode. The magnitude of the ionic current is limited by the barrier layer. When the bias voltage in the conduction direction is below a certain threshold, it fails to provide the necessary

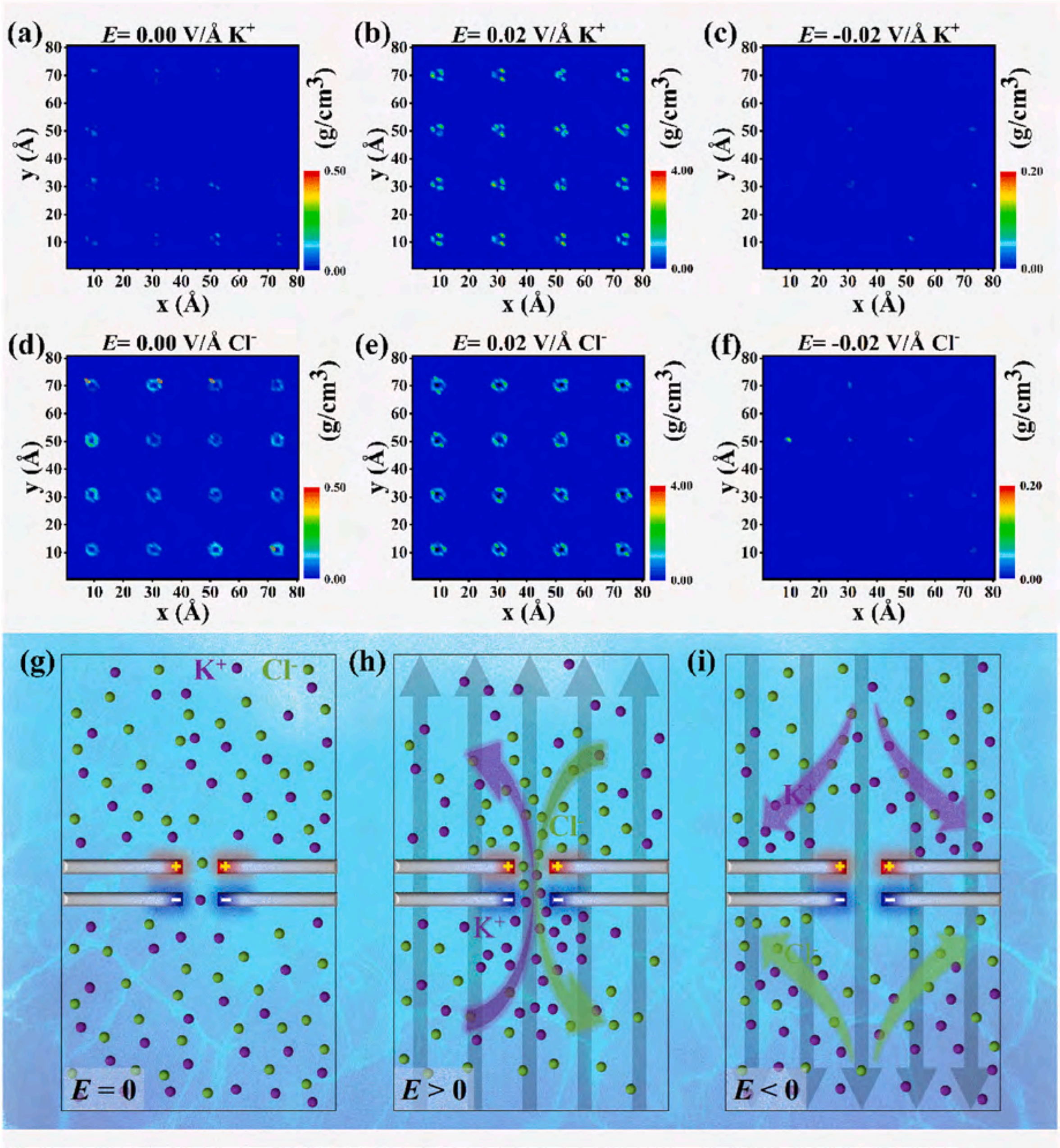

Fig. 6. The 2D mass density distribution on the XY plane, ranging from 49.0 to 56.8 Å along the z-axis, of K^+ and Cl^- in the BOBCV-S system. K^+ density distributions under (a) zero, (b) forward and (c) reverse biases. Cl^- mass density distributions under (d) zero, (e) forward, and (f) reverse biases. Representative snapshots of ion transport through the bilayer asymmetric graphene defects under (g) zero, (h) forward, and (i) reverse biases.

energy for the charge carriers to overcome the barrier layer, leading to either a small current or no current. As the voltage increases, charge carriers acquire sufficient energy to penetrate the barrier layer, leading to a significant ion flow. These findings contribute to our understanding of the mechanisms driving ion current rectification in asymmetric nanopores and highlight the potential application in various nanoscale ion transport channels.

4. Conclusions

Heterogeneous membranes composed of bilayer charged graphene are designed for high-efficiency ion current rectification (ICR). The hybrid nanochannel BOBCV-S with both structural and charge asymmetry exhibits selective transport of K^+ and Cl^- as well as ion current rectification with a remarkable switching ratio of 10^2. The asymmetric factors in the nanochannels lead to ion current unidirectional conduction by controlling the concentration of carriers in the nanopores. The findings and theoretical understanding pave the way for the design and fabrication of nanoscale ion diodes.

Credit author statement

Yanbo Xin designed the methodology, created the models, analyzed the data, conceived the manuscript concept and wrote the manuscript. Anping Huang, Qin Gao and Paul K. Chu revised the manuscript and Anping Huang directed the whole work. All the authors discussed the results and commented on the manuscript.

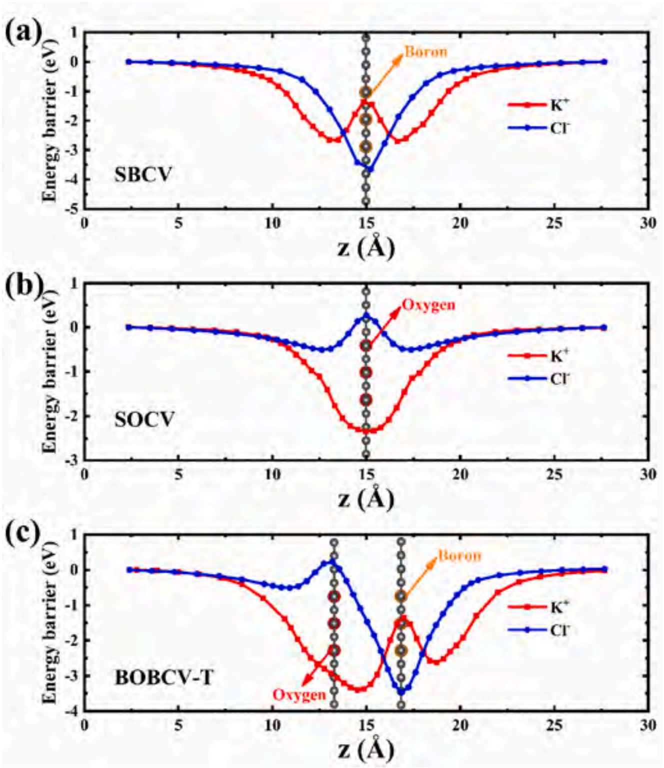

Fig. 7. Energy profile associated with the penetration of K^+ and Cl^- through graphene considering different types of defects. Energy profile for ion penetration in (a) single-layer graphene with B-terminal carbon vacancy (SBCV), (b) single-layer graphene with O-terminal carbon vacancy (SOCV), and (c) bilayer graphene with O-terminal and B-terminal carbon vacancy to the third (BOBCV-T).

Declaration of competing interest

The authors declare that they have no known competing financial interests or personal relationships that could have appeared to influence the work reported in this paper.

Data availability

Data will be made available on request.

Acknowledgments

This research was supported by the National Natural Science Foundation of China (Grant Nos. 51872010 and 61975005), Foundation of Beijing Academy of Quantum Information Sciences (Grant No. Y18G28), City University of Hong Kong Donation Research Grant (DON-RMG No. 9229021), City University of Hong Kong Strategic Research Grant (SRG No. 7005505), as well as City University of Hong Kong Donation Grant (No. 9220061).

Appendix A. Supplementary data

Supplementary data to this article can be found online at https://doi.org/10.1016/j.mtchem.2023.101767.

References

[1] Y. Liu, Y. Chen, Y. Guo, X. Wang, S. Ding, X. Sun, H. Wang, Y. Zhu, L. Jiang, Photo-controllable ion-gated metal-organic framework MIL-53 sub-nanochannels for efficient osmotic energy generation, ACS Nano 16 (2022) 16343–16352, https://doi.org/10.1021/acsnano.2c05498.

[2] Y. Hou, X. Hou, Bioinspired nanofluidic iontronics, Science 373 (2021) 628–629, 80, https://www.science.org/doi/10.1126/science.abj0437.

[3] W. Miao, Y. Tian, L. Jiang, Bioinspired superspreading surface: from essential mechanism to application, Acc. Chem. Res. 55 (2022) 1467–1479, https://doi.org/10.1021/acs.accounts.2c00042.

[4] Y. He, M. Tsutsui, Y. Zhou, X.S. Miao, Solid-state nanopore systems: from materials to applications, NPG Asia Mater. 13 (2021) 48, https://doi.org/10.1038/s41427-021-00313-z.

[5] H. Zhang, X. Li, J. Hou, L. Jiang, H. Wang, Angstrom-scale ion channels towards single-ion selectivity, Chem. Soc. Rev. 51 (2022) 2224–2254, https://doi.org/10.1039/D1CS00582K.

[6] L. Ma, Z. Li, Z. Yuan, C. Huang, Z.S. Siwy, Y. Qiu, Modulation of ionic current rectification in ultrashort conical nanopores, Anal. Chem. 92 (2020) 16188–16196, https://doi.org/10.1021/acs.analchem.0c03989.

[7] N.R. Aluru, F. Aydin, M.Z. Bazant, D. Blankschtein, A.H. Brozena, J.P. de Souza, M. Elimelech, S. Faucher, J.T. Fourkas, V.B. Koman, M. Kuehne, H.J. Kulik, H.-K. Li, Y. Li, Z. Li, A. Majumdar, J. Martis, R.P. Misra, A. Noy, T.A. Pham, H. Qu, A. Rayabharam, M.A. Reed, C.L. Ritt, E. Schwegler, Z. Siwy, M.S. Strano, Y. Wang, Y.-C. Yao, C. Zhan, Z. Zhang, Fluids and electrolytes under confinement in single-digit nanopores, Chem. Rev. 123 (2023) 2737–2831, https://doi.org/10.1021/acs.chemrev.2c00155.

[8] X.-C. Chen, H. Zhang, S.-H. Liu, Y. Zhou, L. Jiang, Engineering polymeric nanofluidic membranes for efficient ionic transport: biomimetic design, material construction, and advanced functionalities, ACS Nano 16 (2022) 17613–17640, https://doi.org/10.1021/acsnano.2c07641.

[9] J. Wang, Y. Zhou, L. Jiang, Bio-inspired track-etched polymeric nanochannels: steady-state biosensors for detection of analytes, ACS Nano 15 (2021) 18974–19013, https://doi.org/10.1021/acsnano.1c08582.

[10] F. Yan, L. Yao, K. Chen, Q. Yang, B. Su, An ultrathin and highly porous silica nanochannel membrane: toward highly efficient salinity energy conversion, J. Mater. Chem. A. 7 (2019) 2385–2391, https://doi.org/10.1039/C8TA10848J.

[11] A. Kiy, S. Dutt, C. Notthoff, M.E. Toimil-Molares, N. Kirby, P. Kluth, Highly rectifying conical nanopores in amorphous SiO_2 membranes for nanofluidic osmotic power generation and electroosmotic pumps, ACS Appl. Nano Mater. 6 (2023) 8564–8573, https://doi.org/10.1021/acsanm.3c00960.

[12] Y. He, L. Huang, B. Song, B. Wu, L. Yan, H. Deng, Z. Yang, W. Yang, H. Wang, Z. Liang, J. Luo, Defluorination by ion exchange of SO_4^{2-} on alumina surface: adsorption mechanism and kinetics, Chemosphere 273 (2021), 129678, https://doi.org/10.1016/j.chemosphere.2021.129678.

[13] Y.-C. Liu, L.-H. Yeh, M.-J. Zheng, K.C.-W. Wu, Highly selective and high-performance osmotic power generators in subnanochannel membranes enabled by metal-organic frameworks, Sci. Adv. 7 (2021) 1–9, https://doi.org/10.1126/sciadv.abe9924.

[14] C. Wang, F. Liu, Z. Tan, Y. Chen, W. Hu, X. Xia, Fabrication of bio-inspired 2D MOFs/PAA hybrid membrane for asymmetric ion transport, Adv. Funct. Mater. 30 (2020), 1908804, https://doi.org/10.1002/adfm.201908804.

[15] X. Zhao, C. Lu, L. Yang, W. Chen, W. Xin, X.-Y. Kong, Q. Fu, L. Wen, G. Qiao, L. Jiang, Metal organic framework enhanced SPEEK/SPSF heterogeneous membrane for ion transport and energy conversion, Nano Energy 81 (2021), 105657, https://doi.org/10.1016/j.nanoen.2020.105657.

[16] L. Yao, Q. Li, S. Pan, J. Cheng, X. Liu, Bio-Inspired salinity-gradient power generation with UiO-66-NH_2 metal-organic framework based composite membrane, Front. Bioeng. Biotechnol. 10 (2022) 1–9, https://doi.org/10.3389/fbioe.2022.901507.

[17] F. Sheng, B. Wu, X. Li, T. Xu, M.A. Shehzad, X. Wang, L. Ge, H. Wang, T. Xu, Efficient ion sieving in covalent organic framework membranes with sub-2-nanometer channels, Adv. Mater. 33 (2021), 2104404, https://doi.org/10.1002/adma.202104404.

[18] P. Zhang, S. Chen, C. Zhu, L. Hou, W. Xian, X. Zuo, Q. Zhang, L. Zhang, S. Ma, Q. Sun, Covalent organic framework nanofluidic membrane as a platform for highly sensitive bionic thermosensation, Nat. Commun. 12 (2021) 1844, https://doi.org/10.1038/s41467-021-22141-z.

[19] S. Zhao, C. Jiang, J. Fan, S. Hong, P. Mei, R. Yao, Y. Liu, S. Zhang, H. Li, H. Zhang, C. Sun, Z. Guo, P. Shao, Y. Zhu, J. Zhang, L. Guo, Y. Ma, J. Zhang, X. Feng, F. Wang, H. Wu, B. Wang, Hydrophilicity gradient in covalent organic frameworks for membrane distillation, Nat. Mater. 20 (2021) 1551–1558, https://doi.org/10.1038/s41563-021-01052-w.

[20] X. Yu, C. Li, J. Chang, Y. Wang, W. Xia, J. Suo, X. Guan, V. Valtchev, Y. Yan, S. Qiu, Q. Fang, Gating effects for ion transport in three-dimensional functionalized covalent organic frameworks, Angew. Chemie Int. Ed. 61 (2022), https://doi.org/10.1002/anie.202200820, 1–7.

[21] Y. Song, C. Zhu, S. Ma, Advanced porous organic polymer membranes: design, fabrication, and energy-saving applications, EnergyChem 4 (2022), 100079, https://doi.org/10.1016/j.enchem.2022.100079.

[22] L. Cao, I.-C. Chen, X. Liu, Z. Li, Z. Zhou, Z. Lai, An ionic diode covalent organic framework membrane for efficient osmotic energy conversion, ACS Nano 16 (2022) 18910–18920, https://doi.org/10.1021/acsnano.2c07813.

[23] P. Robin, T. Emmerich, A. Ismail, A. Niguès, Y. You, G.H. Nam, A. Keerthi, A. Siria, A.K. Geim, B. Radha, L. Bocquet, Long-term memory and synapse-like dynamics in two-dimensional nanofluidic channels, Science 379 (2023) 161–167, https://doi.org/10.1126/science.adc9931, 80.

[24] B. Luan, R. Zhou, Atomic-scale fluidic diodes based on triangular nanopores in bilayer hexagonal boron nitride, Nano Lett. 19 (2019) 977–982, https://doi.org/10.1021/acs.nanolett.8b04208.

[25] A. Kochaev, K. Katin, M. Maslov, On ionic transport through pores in a borophene–graphene membrane, Mater. Today Chem. 30 (2023), 101512, https://doi.org/10.1016/j.mtchem.2023.101512.

[26] J. Wang, H. Zhou, S. Li, L. Wang, Selective ion transport in two-dimensional lamellar nanochannel membranes, Angew. Chemie Int. Ed. 62 (2023), https://doi.org/10.1002/anie.202218321, 1–22.

[27] A. Smolyanitsky, E. Paulechka, K. Kroenlein, Aqueous ion trapping and transport in graphene-embedded 18-crown-6 ether pores, ACS Nano 12 (2018) 6677–6684, https://doi.org/10.1021/acsnano.8b01692.

[28] K. Sun, O.J. Silveira, S. Saito, K. Sagisaka, S. Yamaguchi, A.S. Foster, S. Kawai, Manipulation of spin polarization in boron-substituted graphene nanoribbons, ACS Nano 16 (2022) 11244–11250, https://doi.org/10.1021/acsnano.2c04563.

[29] G. Kresse, J. Furthmüller, Efficient iterative schemes for ab initio total-energy calculations using a plane-wave basis set, Phys. Rev. B - Condens. Matter Mater. Phys. 54 (1996) 11169–11186, https://doi.org/10.1103/PhysRevB.54.11169.

[30] J.P. Perdew, K. Burke, M. Ernzerhof, Generalized gradient approximation made simple, Phys. Rev. Lett. 77 (1996) 3865–3868, https://doi.org/10.1103/PhysRevLett.77.3865.

[31] G. Henkelman, H. Jónsson, Improved tangent estimate in the nudged elastic band method for finding minimum energy paths and saddle points, J. Chem. Phys. 113 (2000) 9978–9985, https://doi.org/10.1063/1.1323224.

[32] A. Allouche, Software news and updates gabedit — a graphical user interface for computational chemistry softwares, J. Comput. Chem. 32 (2012) 174–182, https://doi.org/10.1002/jcc.

[33] H. Jnsson, G. Mills, K.W. Jacobsen, Nudged Elastic Band Method for Finding Minimum Energy Paths of Transitions, World Sci., 1998, pp. 385–404.

[34] D. Sheppard, P. Xiao, W. Chemelewski, D.D. Johnson, G. Henkelman, A generalized solid-state nudged elastic band method, J. Chem. Phys. 136 (2012), 074103, https://doi.org/10.1063/1.3684549.

[35] P. Trucano, R. Chen, Structure of graphite by neutron diffraction, Nature 258 (1975) 136–137, https://doi.org/10.1038/258136a0.

[36] K. Momma, F. Izumi, VESTA 3 for three-dimensional visualization of crystal, volumetric and morphology data, J. Appl. Crystallogr. 44 (2011) 1272–1276, https://doi.org/10.1107/S0021889811038970.

[37] D. Tou, K. Berka, J. Ko, R. Svobodov, Atomic Charge Calculator II : web-based tool for the ′ s, Tom a 48 (2020) 591–596, https://doi.org/10.1093/nar/gkaa367.

[38] A. Kochaev, K. Katin, M. Maslov, On ionic transport through pores in a borophene–graphene membrane, Mater. Today Chem. 30 (2023), 101512, https://doi.org/10.1016/j.mtchem.2023.101512.

[39] W.L. Jorgensen, J. Chandrasekhar, J.D. Madura, R.W. Impey, M.L. Klein, Comparison of simple potential functions for simulating liquid water, J. Chem. Phys. 79 (1983) 926–935, https://doi.org/10.1063/1.445869.

[40] E. Neria, S. Fischer, M. Karplus, Simulation of activation free energies in molecular systems, J. Chem. Phys. 105 (1996) 1902–1921, https://doi.org/10.1063/1.472061.

[41] A.P. Thompson, H.M. Aktulga, R. Berger, D.S. Bolintineanu, W.M. Brown, P. S. Crozier, J. Pieter, A. Kohlmeyer, S.G. Moore, T. Dac, R. Shan, M.J. Stevens, J. Tranchida, C. Trott, S.J. Plimpton, Feature article LAMMPS - a flexible simulation tool for particle-based materials modeling at the atomic , meso , and continuum scales, Comput. Phys. Commun. 271 (2022), 108171, https://doi.org/10.1016/j.cpc.2021.108171.

[42] S. Plimpton, Fast parallel algorithms for short-range molecular dynamics, J. Comput. Phys. 117 (1995) 1–19, https://doi.org/10.1006/jcph.1995.1039.

[43] Y. Xin, A. Huang, Q. Hu, H. Shi, M. Wang, Z. Xiao, X. Zheng, Z. Di, P.K. Chu, Barrier reduction of lithium ion tunneling through graphene with hybrid defects: first-principles calculations, Adv. Theory Simulations 1 (2018), 1700009, https://doi.org/10.1002/adts.201700009.

[44] S. Hu, M. Lozada-Hidalgo, F.C. Wang, A. Mishchenko, F. Schedin, R.R. Nair, E. W. Hill, D.W. Boukhvalov, M.I. Katsnelson, R.A.W. Dryfe, I.V. Grigorieva, H.A. Wu, A.K. Geim, Proton transport through one-atom-thick crystals, Nature 516 (2014) 227–230, https://doi.org/10.1038/nature14015.

[45] F. Xiong, Y. Jiang, L. Cheng, R. Yu, S. Tan, C. Tang, C. Zuo, Q. An, Y. Zhao, J. Gaumet, L. Mai, Low-strain TiP_2O_7 with three-dimensional ion channels as long-life and high-rate anode material for Mg-ion batteries, Interdiscip. Mater. 1 (2022) 140–147, https://doi.org/10.1002/idm2.12004.

[46] Y. Hao, F. Hu, Y. Chen, Y. Wang, J. Xue, S. Yang, S. Peng, Recent progress of electrospun nanofibers for zinc–air batteries, Adv. Fiber Mater. 4 (2022) 185–202, https://doi.org/10.1007/s42765-021-00109-4.

[47] H. Wang, L. Su, M. Yagmurcukardes, J. Chen, Y. Jiang, Z. Li, A. Quan, F.M. Peeters, C. Wang, A.K. Geim, S. Hu, Blue energy conversion from holey-graphene-like membranes with a high density of subnanometer pores, Nano Lett. 20 (2020) 8634–8639, https://doi.org/10.1021/acs.nanolett.0c03342.

[48] Y. Ding, M. Zeng, Q. Zheng, J. Zhang, D. Xu, W. Chen, C. Wang, S. Chen, Y. Xie, Y. Ding, S. Zheng, J. Zhao, P. Gao, L. Fu, Bidirectional and reversible tuning of the interlayer spacing of two-dimensional materials, Nat. Commun. 12 (2021) 5886, https://doi.org/10.1038/s41467-021-26139-5.

[49] B. Tang, Y. Zhao, Z. Wang, S. Chen, Y. Wu, Y. Tseng, L. Li, Y. Guo, Z. Zhou, S.-H. Bo, Ultrathin salt-free polymer-in-ceramic electrolyte for solid-state sodium batteries, eScience 1 (2021) 194–202, https://doi.org/10.1016/j.esci.2021.12.001.

[50] K. Xie, K. Ren, Q. Wang, Y. Lin, F. Ma, C. Sun, Y. Li, X. Zhao, C. Lai, In situ construction of zinc-rich polymeric solid–electrolyte interface for high-performance zinc anode, eScience 3 (2023), 100153, https://doi.org/10.1016/j.esci.2023.100153.

Supporting Information

Controllable Ion Transport by Bilayer Graphene with Charged Nanopores

*Yanbo Xin,[1] Qin Gao,[2] Jiangshun Huang,[1] Juan Gao,[1] Xueli Geng,[1] Hongliang Shi,[1] Mei Wang,[1] Zhisong Xiao,[1] Paul K. Chu,[3] Anping Huang[1]**

[1] School of Physics, Beihang University, Beijing 100191, China

[2] School of Physics and School of Chemistry, Beihang University, Beijing 100191, China

[3] Department of Physics, Department of Materials Science and Engineering, and Department of Biomedical Engineering, City University of Hong Kong, Tat Chee Avenue, Kowloon, Hong Kong, China

** Corresponding Authors*

Anping Huang − Email: aphuang@buaa.edu.cn (Dr. A. P. Huang)

School of Physics, Beihang University, Beijing 100191, China

Table of contents

1. The crystal structure and atomic charges of nanopores in bilayer graphene

Asymmetric double-layer graphene stacks with charged nanopores are constructed. Six types of nanochannels, bilayer graphene with carbon vacancy to the first (BCV-F), bilayer graphene with carbon vacancy to the second (BCV-S), bilayer graphene with oxygen- and boron-terminated carbon vacancy to the first (BOBCV-F), bilayer graphene with oxygen- and boron-terminated carbon vacancy to the second (BOBCV-S), single-layer graphene with oxygen-terminated carbon vacancy (SOCV), and single-layer graphene with boron-terminated carbon vacancy (SBCV) , are listed as shown in Figure S1. The separation distance between the two charged graphene nanosheets is determined to be 3.80 Å using first principles method. To determine the partial atomic charges, the Atom Charge Calculator II (ACC II) with the EQeq method is employed, as depicted in Figure S1.[1]

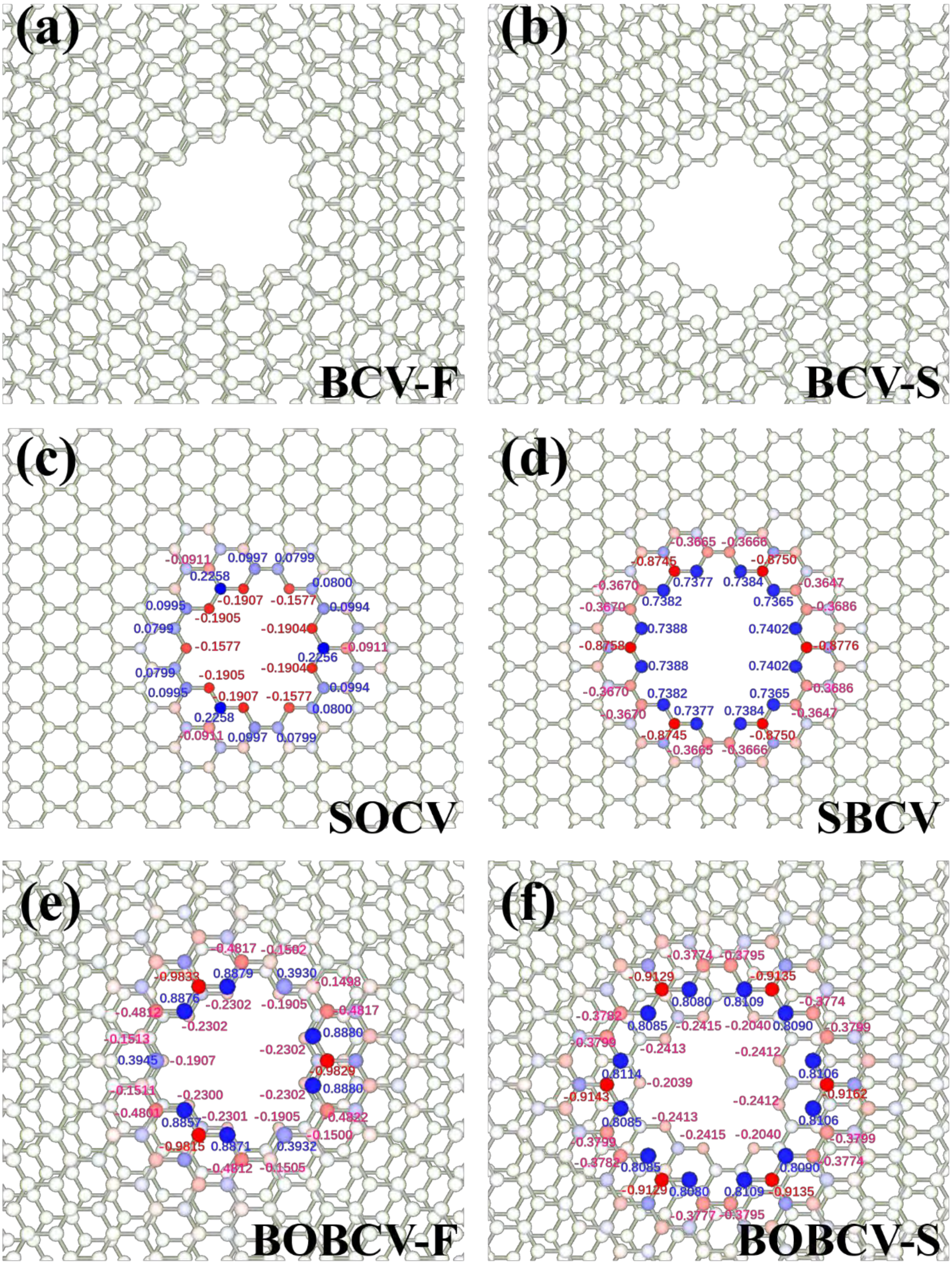

Figure S1. The structure and charge distribution of (a) BCV-F, (b) BCV-S, (c) SOCV, (d) SBCV, (e) BOBCV-F, and (f) BOBCV-S. Red balls represent oxygen atoms, pink balls represent boron atoms, and gray balls represent carbon atoms.

2. The Lennard Jones and force field parameters

Table S1. The Lennard Jones and force field parameters adopted in this work. [2]

	Atom	σ/nm	ε/KJ•mol^{-1}
Water	O-O	3.1656	0.1554
	H-H	0.0000	0.0000
Graphene Nanopores	C-C	3.3900	0.0692
	C-O	3.4360	0.0850
	C-B	3.5342	0.1375
Ions	K-K	2.8400	0.4300
	Cl-Cl	4.8305	0.0128

3. Ionic radii of K^+ and Cl^- ions

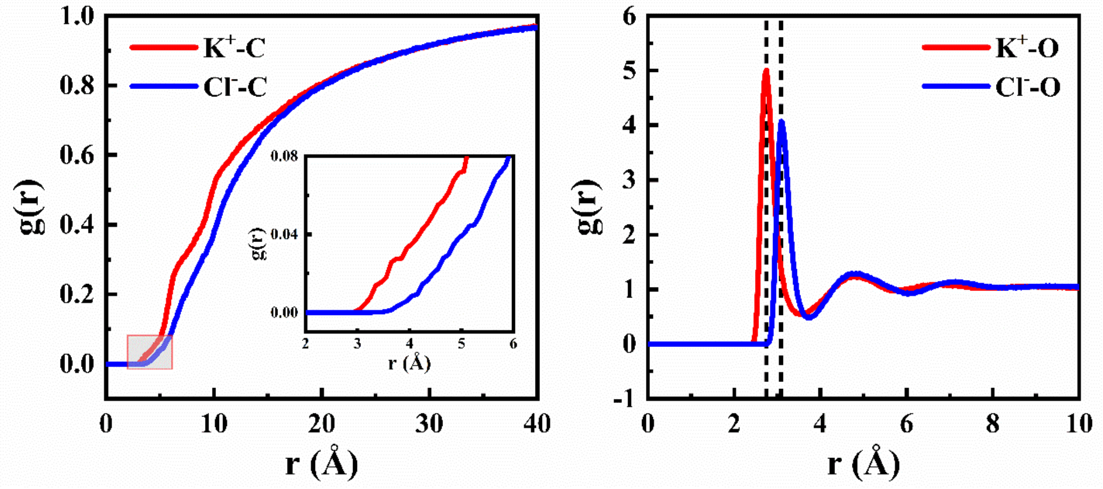

Figure S2. (a) The radial distribution function between ions and carbon atoms on graphene. (b) The radial distribution function between ions and oxygen atoms on H_2O.

The radial distribution function of K^+ ions and Cl^- ions along the carbon atom shows that the distribution of K^+ ions are closer to the carbon atom, as shown in Figure S2 (a). The hydration radii for of K^+ ions and Cl^- ions can refer to the radial distribution function of oxygen atoms on water molecules around the ions. The radial distribution function (RDF) between ions and oxygen atoms on H_2O shows that the RDF curves of K^+ ion and Cl^- ion have two ups and downs, which means that both ions have obvious primary hydration and secondary hydration shells. The hydration radii for K^+ and Cl^- ion are at the first peak, which are ~2.7 Å and ~3.1 Å respectively, as shown in Figure S2 (b).

4. Trapping behavior of ions BCV-F and BCV-S

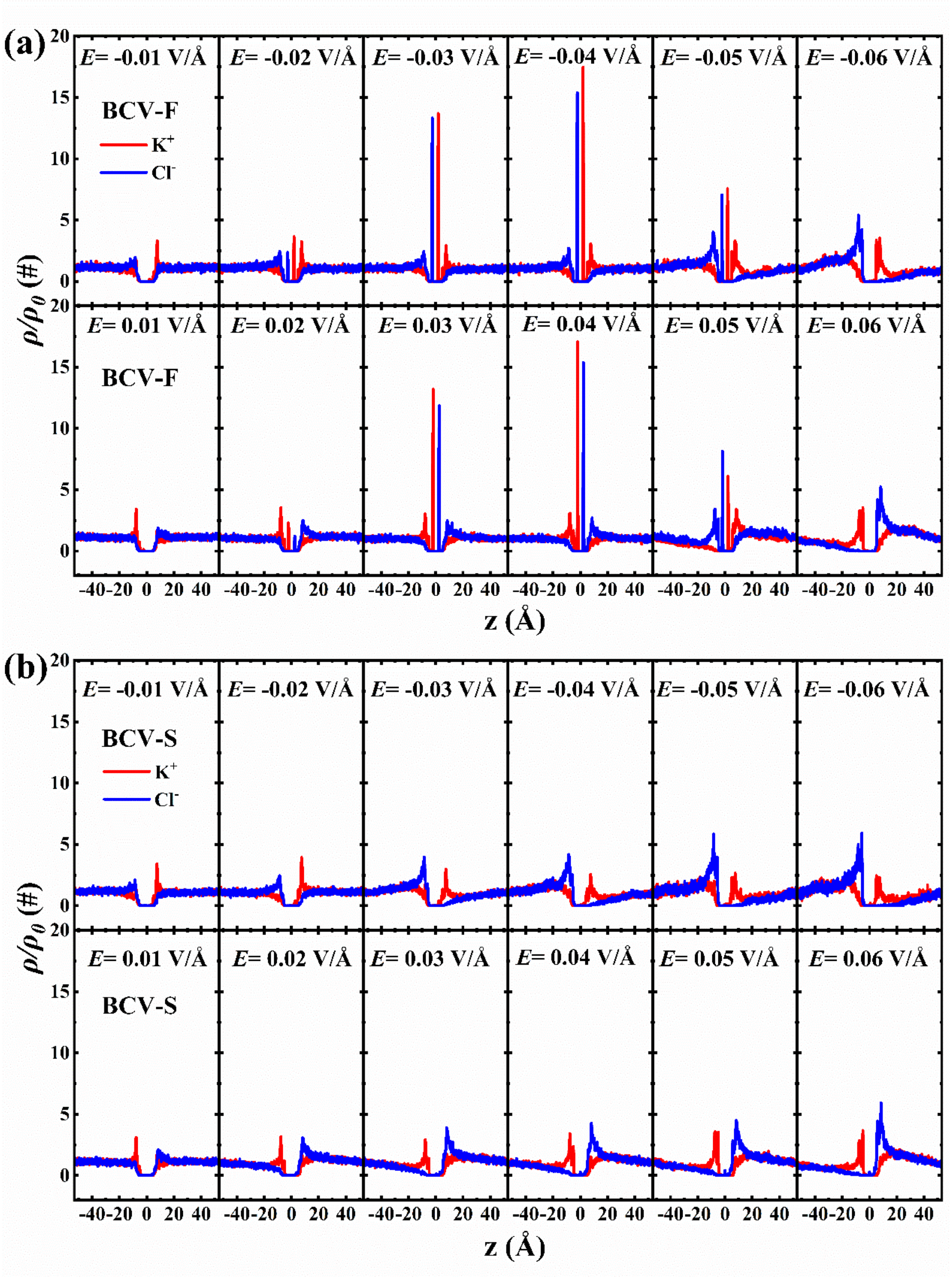

Figure S3. Distribution of ions along the *z*-direction in (a) BCV-F and (b) BCV-S at different applied biasing voltages.

5. Simple logic for nanofluidic computing

The quantity of trapped charge in the nanopores is influenced by the applied positive transmembrane voltage, given a specific concentration of the KCl solution. When a transmembrane field of 0 V/Å is applied, no charges are trapped in the two layers of nanopores in BOBCV-S. As the positive transmembrane voltage gradually increases to approximately 0.02 V/Å, the amount of charge trapped in the nanopores increases gradually. Specifically, K^+ ions are trapped in the negatively charged nanopores, while Cl^- ions are trapped in the positively charged nanopores. Further elevation of the transmembrane voltage leads to a gradual reduction in the amount of trapped charge in the nanopores, as illustrated in by increasing the positive bias, ion trapping in the nanopores initially increases and then decreases, as shown in Figure S4 (a). Notably, in states of high charge trapping, the trapped ions within the nanopores are rapidly released upon removal of the transmembrane voltage, returning to the zero-voltage charge trapping state. This input-output relationship exhibits the characteristics of NOT logic gates or operations, where the ions within the nanopores are expelled when the bias is removed, as depicted in Figure S4 (b). Building upon the two asymmetric structures, the NOT gate can be utilized to realize AND, OR, and XOR gates, as demonstrated in Figure S4 (c).

The switching speed of nanopore rectifiers from the cutoff state (negative bias) to the conducting state (positive bias) can be estimated. The ionic response can be understood as the directed diffusion of ions in an aqueous solution towards the charged nanopore followed by the ion's escape from the confinement across the membrane. The effective average transition time τ, $\tau = \tau_a + \tau_m$, where τ_a is the ion's association time with the charged nanopore in the aqueous solution, and τ_m is the ion's transmembrane penetration time. Under positive low bias, some ions cannot overcome the barrier of the boron nanopore after associating with the charged nanopore, resulting in $\tau_a \ll \tau_m$. Under positive high bias, τ_m finally becomes smaller than τ_a, and the ionic current is limited by the saturation value of association. In conclusion, both the ionic rectification response speed and the response speed of charged nanopore trapping of ions are related to the association time τ_a of the hydrated ion with the charged nanopore. Its order of magnitude can be estimated by the following formula: $\tau_a \sim q/I$, where q is the charge of the trapped ion in the nanopore, such as K^+, and I is the corresponding ionic current, corresponding to K^+ ions. For the defects (O9B12) nanopore structure given here, the response time can be referred to τ_a ~ a few nanoseconds under 0.02V/A bias.

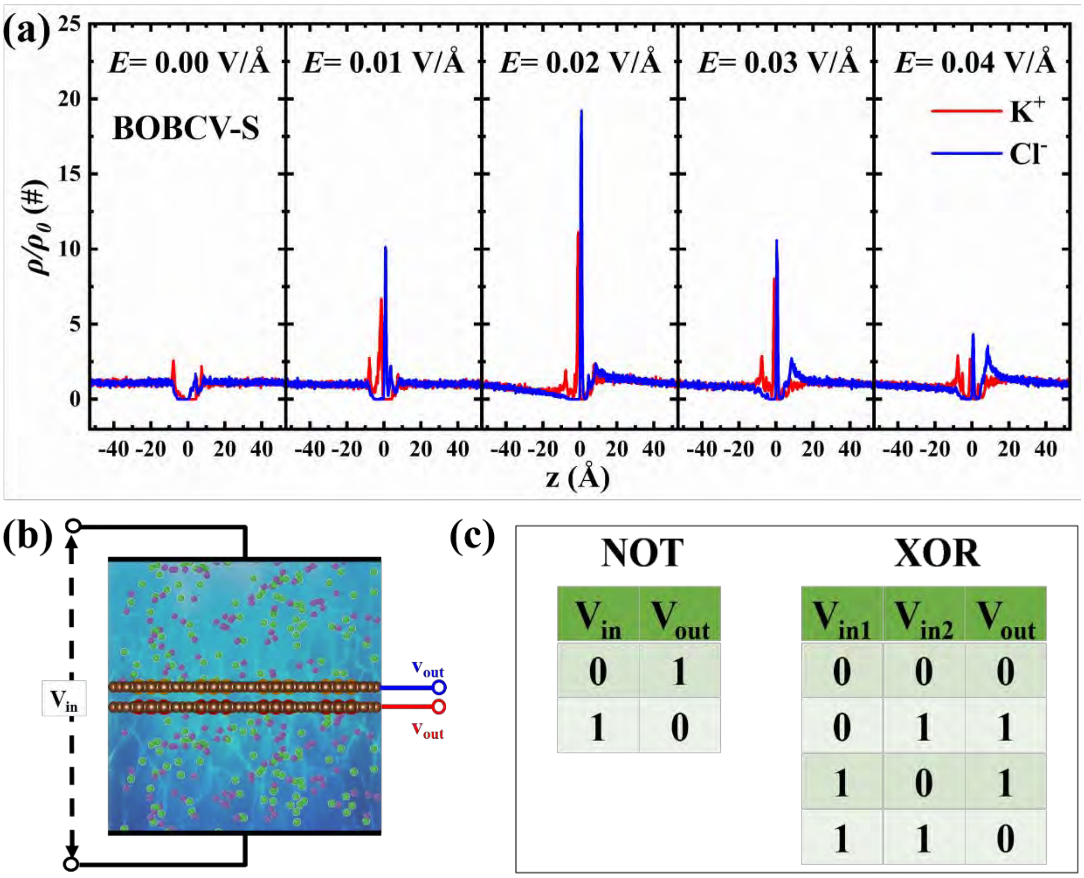

V_{in}	V_{out}
0	1
1	0

V_{in1}	V_{in2}	V_{out}
0	0	0
0	1	1
1	0	1
1	1	0

Figure S4. (a) Distribution of ions along the *z*-direction through bilayer graphene containing defects (O9B12) at different applied biasing voltages. (b) Structure diagram of logic device input and output. (c) Simple logical operations including NOT, exclusive AND, RO, and XOR are obtained by measuring the effective membrane potential in both the "on" and "off" permeation modes.

6. Calculation of rectification ratio of fluid diodes

To ascertain the rectification ratio of a fluid diode, it is imperative to compute the ratio between the forward flow rate and the reverse flow rate. This ratio serves as a quantitative measure of the diode's effectiveness in facilitating fluid flow in one direction while inhibiting flow in the opposite direction. In the context of ionic current, the following equation can be employed: $I = \sum_i q_i v_i / H$, where I represents the ionic current, H denotes the height of the simulated system, and q_i and v_i correspond to the charge and velocity of the $i - th$ ion, respectively. To calculate the rectification ratio, the forward flow rate ($I_{+\mathrm{j}}$) is divided by the reverse flow rate ($I_{-\mathrm{j}}$), yielding the desired ratio. Here, the symbol j signifies the magnitude of the externally applied bias voltage. This study presents Figure S5, which showcases the ion switches observed in various nanopores of double-layer graphene under distinct ion biases.

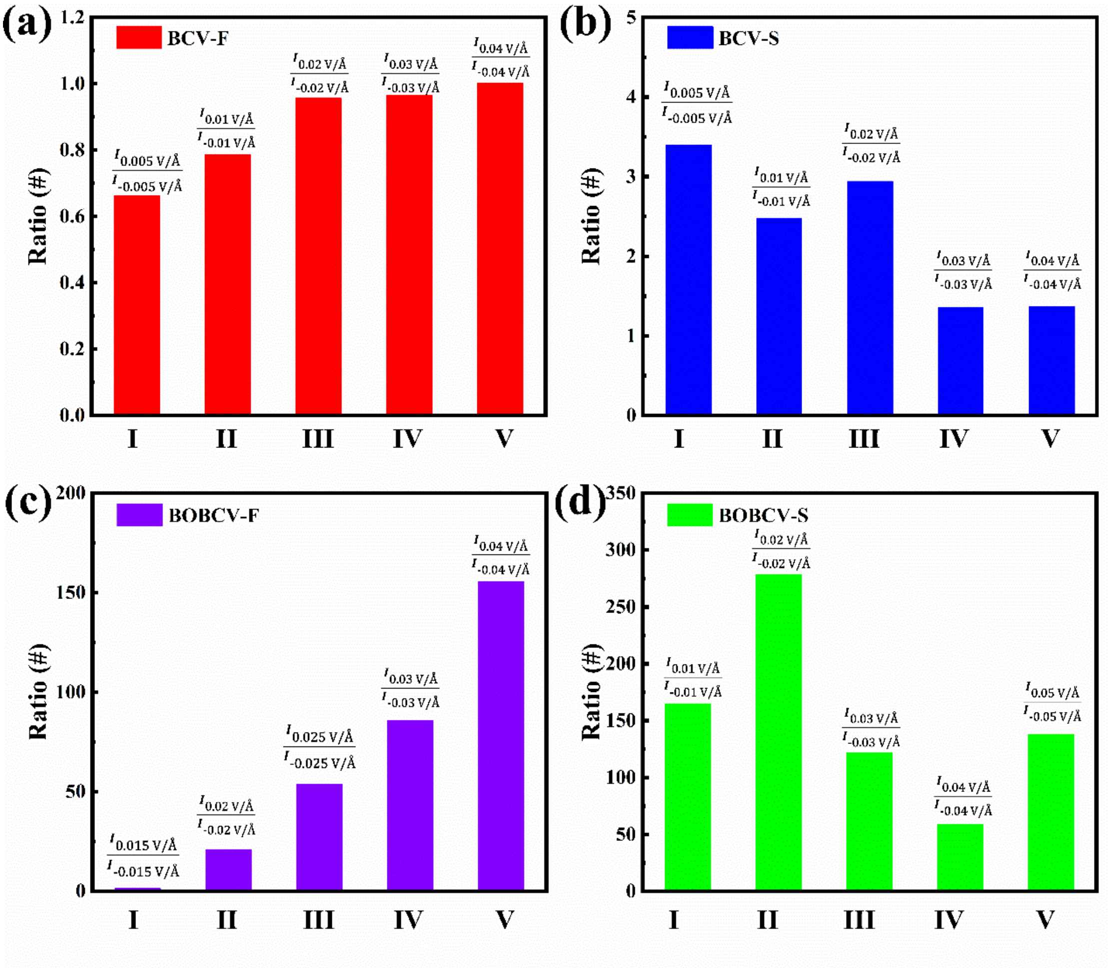

Figure S5. The rectifier switching ratios of bilayer graphene nanopore defects under varying bias voltages. Specifically, (a), (b), (c), and (d) demonstrate the rectifier switching ratio in BCV-F, BCV-S, BOBCV-F and BOBCV-S system.

7. Ionic currents through bilayer graphene with pores

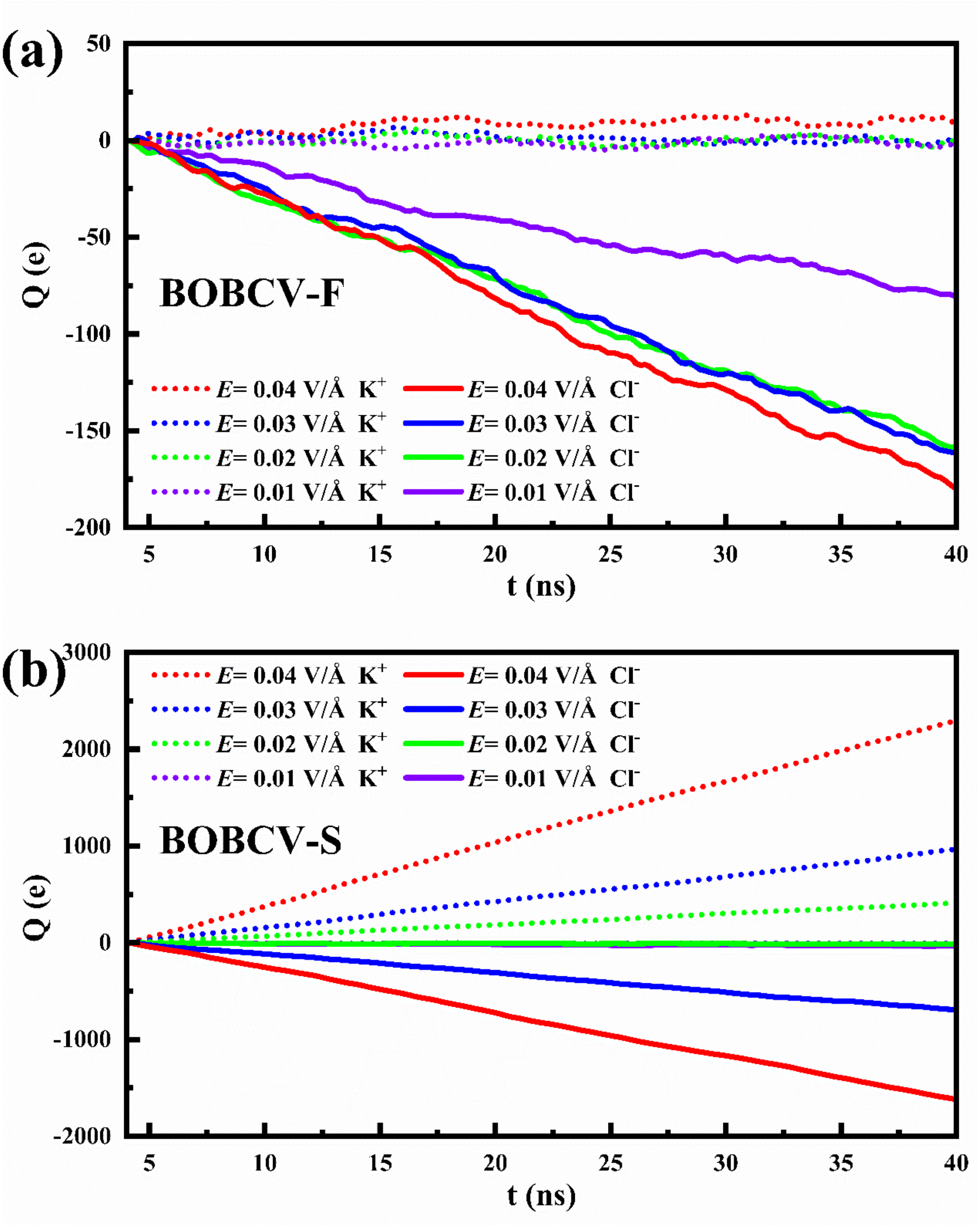

Figure S6. Ionic currents for both K^+ ions and Cl^- ions in (a) BOBCV-F system and (b) BOBCV-S system.

8. Time dependence of ion trapping behavior

The time-dependent behavior of ion trapping in defect bilayer graphene is investigated under a positive bias of $E = 0.02$ V/Å. It is observed that an increased interlayer distance of BOBCV-S leads to an extended time required to reach the peak ion trapping. In the case of an interlayer distance of 3.8 Å, as depicted in Figure S7 (a), the saturation time within the nanopore is approximately 1.5 ns. However, for an interlayer distance of 7.6 Å, as shown in Figure S8 (a), the saturation time within the nanopore is approximately 10 ns. Following a continuous thermal equilibration period of 40 ns in the simulations, the applied bias is removed, resulting in the de-trapping of ions from within the nanopores and their return to the surrounding solution. This de-trapping process is illustrated in Figures S7 (b) and S8 (b). By examining the time dependence of ion trapping, these findings contribute to a deeper understanding of the behavior of ions within defect bilayer graphene structures, providing valuable insights for related applications.

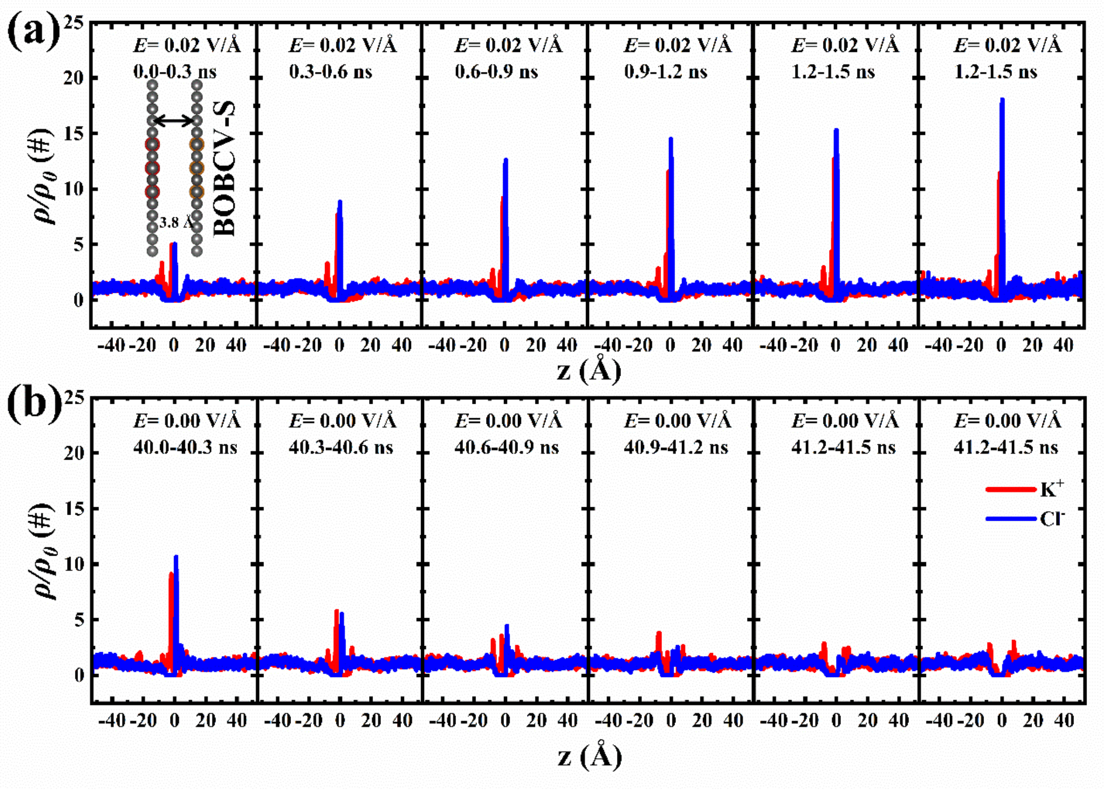

Figure S7. Time dependence of ion trapping behavior in BOBCV-S under a positive bias of *E* = 0.02 V/Å. (a) The progressive accumulation of ions within the defects over time. (b) Ion desorption process within the defects when the positive bias voltage is switched off (*E* = 0.00 V/Å).

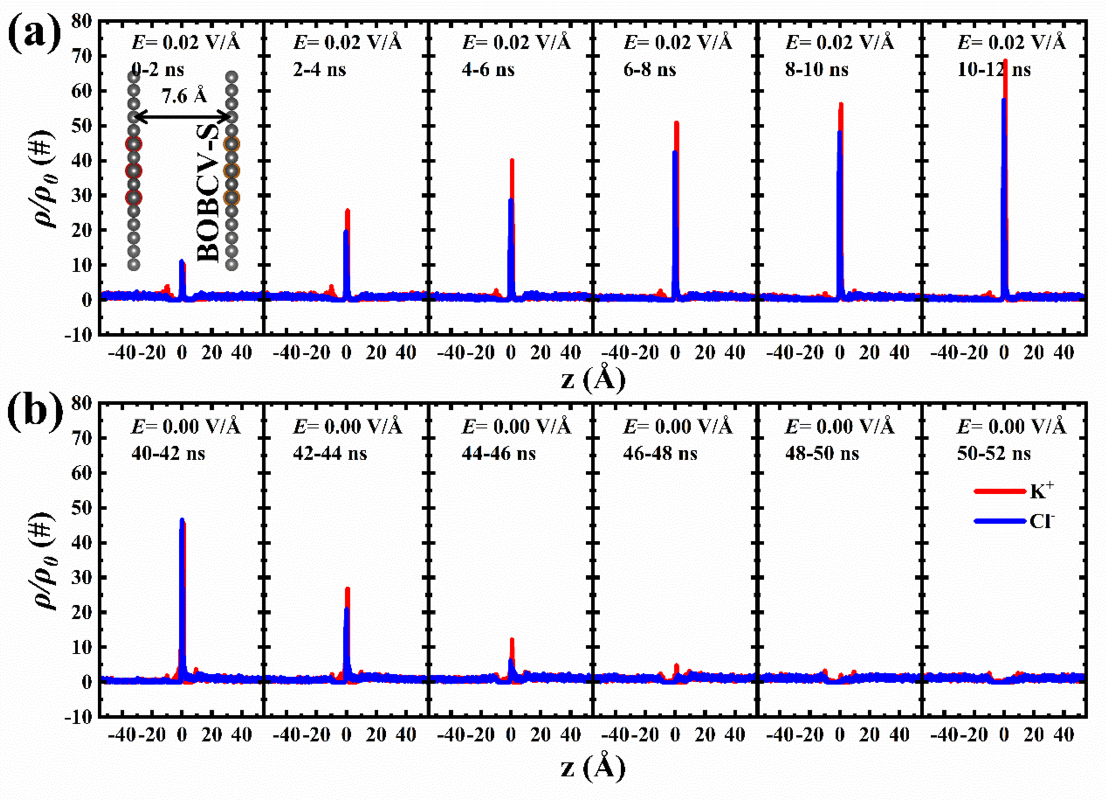

Figure S8. Time dependence of ion trapping behavior in BOBCV-S under a positive bias of *E* = 0.02 V/Å. (a) The progressive accumulation of ions within the defects over time. (b) Ion desorption process within the defects when the positive bias voltage is switched off (*E* = 0.00 V/Å).

9. Ion transport in single-layer graphene with defects

Single-layer graphene with O-terminal carbon vacancy (SOCV) and B-terminal carbon vacancy (SBCV) are immersed in an aqueous solution, and an external bias voltage is applied to measure their ionic currents. The results revealed distinct ion transport characteristics for the two types of nanopores. In the case of the oxygen-terminated nanopore, K^+ ions permeate the pore, forming a K^+ ion current, while Cl^- ions are unable to pass through the nanopore, resulting in the absence of a chloride ion current, as depicted in Figure S9 (a). Conversely, in the boron-terminated nanopore, chloride ions traverse the pore, creating a chloride ion current, whereas K^+ ions are hindered from passing through, leading to the absence of a K^+ ion current, as shown in Figure S9 (b). These findings demonstrate the selective permeability of the nanopores based on their terminal atoms, highlighting the differential behavior of K^+ and Cl^- ions in the graphene nanopore system.

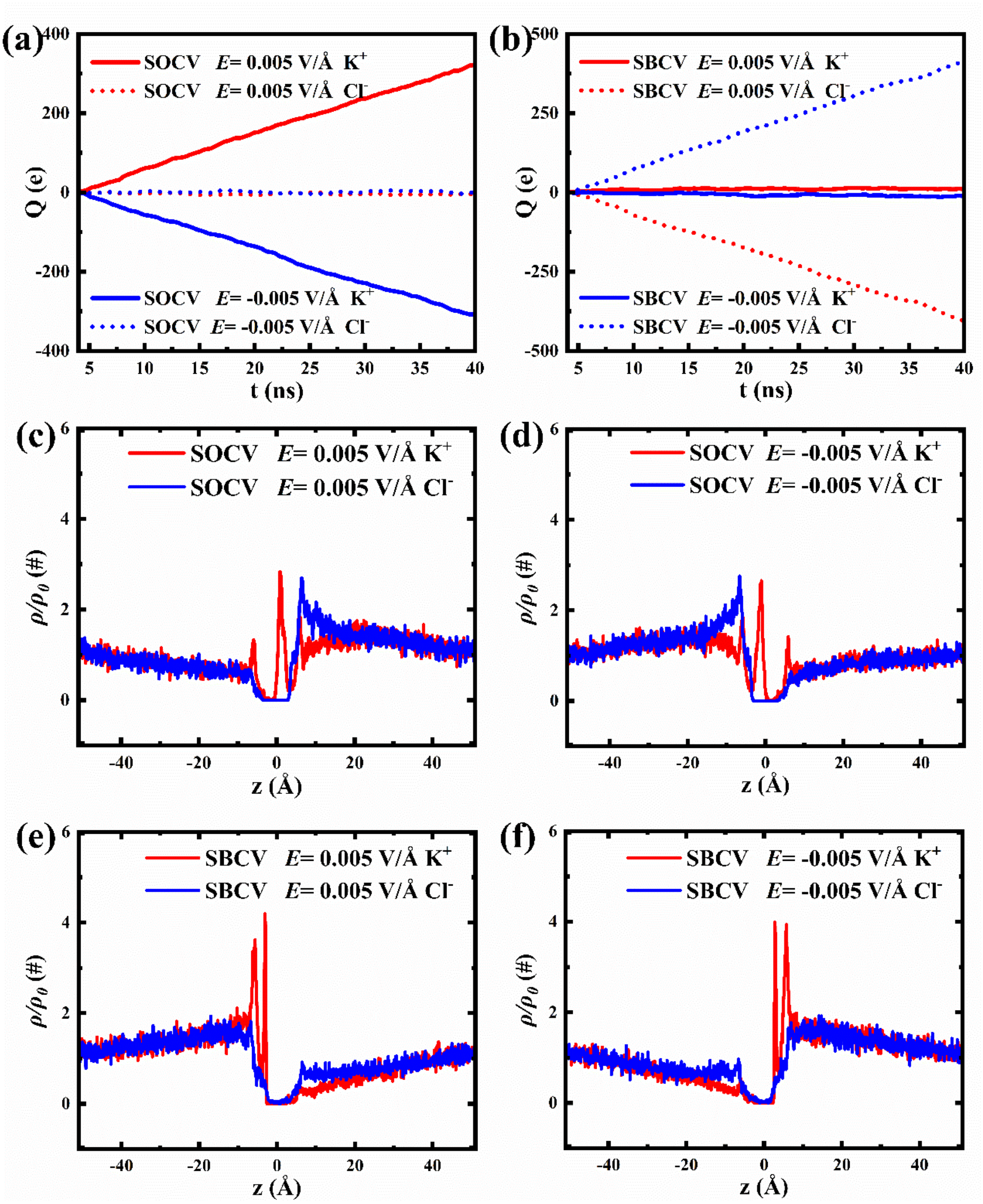

Figure S9. Ionic currents through single-layer graphene with (a) SOCV and (b) SBCV respectively. (c), (d), (e), and (f) present the distribution of ions along the *z*-direction through SOCV and SBCV at different biasing voltages (*E* = -0.005V/Å and *E* = 0.005V/Å).

References

[1] D. Tou, K. Berka, J. Ko, R. Svobodov, Atomic Charge Calculator II: web-based tool for the calculation of partial atomic charges, 48 (2020) 591–596. https://doi.org/10.1093/nar/gkaa367.

[2] A. Kochaev, K. Katin, M. Maslov, On ionic transport through pores in a borophene–graphene membrane, Mater. Today Chem. 30 (2023) 101512. https://doi.org/10.1016/j.mtchem.2023.101512.